J Ther Eng, Vol. 9, No. 3, pp. 614−636, May, 2023

Journal of Thermal Engineering
Web page info: https://jten.yildiz.edu.tr
DOI: 10.18186/thermal.1297556

Journal of Thermal Engineering

Research Article

A numerical investigation on thermal analysis of RPC based solar thermochemical reactor for two-step H_2O splitting cycle for hydrogen production

Jeet Prakash SHARMA[1], Ravindra JILTE[1,*], Ravinder KUMAR[1]

[1]*School of Mechanical Engineering, Lovely Professional University, Punjab, 144411, India*

ARTICLE INFO

Article history
Received: 15 April 2021
Accepted: 08 July 2021

Keywords:
Solar Thermochemical; Hydrogen Production; RPC Thickness; Gas Flow Gap; Two-Step Water Splitting Process

ABSTRACT

Ceria based solar thermochemical cycle is a high-temperature based redox chemical reactions to split H_2O or $CO_2$to produce hydrogen and/or syngas. The redox reactions are carried out in a reactor cavity thus the analysis and optimization of design as well as thermal analysis is a crucial factor to improve the solar-to-fuel conversion efficiency. This paper proposes the hybrid design of cylindrical and hemispherical cavity and its effects of geometrical parameters such as reticulated porous ceria (RPC) thickness (*15 mm, 20 mm,* and *25 mm*) and gas flow gap (*5 mm&10 mm*) on temperature and flux distribution and solar-to-fuel efficiency for both steady-state and transient condition. A numerical computational fluid dynamics (CFD) analysis is carried out to study heat and mass transfer as well as geometrical design consideration of the STCR cavity under SolTrace generated Gaussian distributed concentrated solar flux. Two-step water-splitting reaction in the Solar Thermochemical cavity reactor (STCR) using ceria (CeO_2) has been modeled to explore the oxygen evolution/reaction rate and to estimate solar-to-fuel efficiency and its relationship with geometrical factors. The RPC of *25 mm* thickness yields the highest oxygen evolution rate of *0.34 mL/min/gCeO_2* and solar-to-fuel efficiencies are *7.82%, 12.07%* and *16.18%* for *15 mm, 20 mm* and *25 mm* of RPC thickness, respectively without heat recovery. The operating conditions and optimized geometric factors, based on result analysis and comparison, are discussed in detail.

Cite this article as: Sharma JP, Jilte R, Kumar R. A numerical investigation on thermal analysis of RPC based solar thermochemical reactor for two-step H_2O splitting cycle for hydrogen production. J Ther Eng 2023;9(3):614−636.

INTRODUCTION

In the present era, solar energy is the best suited renewable and eternal source of green energy for domestic as well as commercial use. Research and advancement in solar energy over the years have brought solutions to complex problems such as the production of solar fuel i.e. hydrogen and syngas. The solar collector technology has advanced solar energy applications in terms of performance by improving their efficiencies [1, 2]. Solar thermochemical cycles present one of the best possible way for the

***Corresponding author.**
*E-mail address: rdjilte@gmail.com

This paper was recommended for publication in revised form by Regional Editor Ahmet Selim Dalkılıç

production of solar fuels using solar concentrated power. Moreover, this approach also can be integrated with electricity production on the pilot scale. Solar thermochemical processes are used in two major areas: hydrocarbon fuel production and for the production of industrial commodities such as lime and ammonia [3]. Solar thermochemical processes have the major application in hydrocarbon fuel production (from hydrogen and syngas).

Solar thermolysis is the single-step process where H_2O is decomposed into hydrogen and oxygen at the temperature of 2500 K [4]. In this process, the hydrogen and oxygen separation is hard thus it's a highly dangerous process with complicated reaction conditions. Due to the complicacy of the solar thermolysis process, solar thermochemical cycles provide the best-suited alternative of fuel production in a multiple-step reaction system which reduces the temperature requirement. Solar thermochemical cycles were introduced based on the difficulties faced in the solar thermolysis process which requires extremely high temperature and product separation [5]. Primarily, solar thermochemical cycles used metal oxides for hydrogen production in two-steps metal oxide redox reactions. The first step is the reduction step (endothermic) in which metal oxide gets decomposed into metal and releases oxygen at high temperatures. The second step is the oxidation step (exothermic) in which metal oxide reacts with H_2O/CO_2 to produces H_2/CO as a product. Further, hydrogen and syngas can be converted into hydrocarbon fuels via. Fischer-Tropsch process. Since the year 2006, Non-stoichiometric cerium oxide or ceria (CeO_2) has emerged as one of the best-suited redox material [6, 7] for the solar thermochemical cycle due to its high oxygen solid-state conductivity, fast redox kinetics and crystallographic stability. The redox reactions for two-step H_2O/CO_2-splitting solar thermochemical cycle based on non-stoichiometric ceria has been given as:

High-temperature reduction:

$$CeO_2 \xrightarrow{+\Delta H} CeO_{(2-\delta)} + \frac{\delta}{2} O_2 \tag{1}$$

Low-temperature oxidation (with H_2O):

$$CeO_{(2-\delta)} + \delta H_2O \xrightarrow{-\Delta H} CeO_2 + \delta H_2 \tag{2}$$

Low-temperature oxidation (with CO_2):

$$CeO_{(2-\delta)} + \delta CO_2 \xrightarrow{-\Delta H} CeO_2 + \delta CO \tag{3}$$

The first step is known as the reduction step which takes place at high temperature. In this step, ceria gets reduced to a non-stoichiometric state by solar concentrated energy. After the reduction step, the low-temperature oxidation step takes place. In this step, ceria is re-oxidized by reacting with water and/or CO_2 and produces H_2 and/or CO. These redox reactions take place in the solar reactor cavity receiver. These cavity receivers can be designed in various ways according to the requirement such as stationary or rotating [8–10], aerosol flow reactors [11], glass dome reactors [12] and moving and fluidized bed reactors [13, 14]. Water slitting process was demonstrated using monolithic reactors of 50 kW power and yearly performance of solar thermochemical plant was investigated. It was concluded that with advanced strategies the overall performance can be improved up to 46% [15]. A transient heat transfer model of solar thermochemical reactor of reticulated porous ceramic was investigated. Results of the numerical study show that the RPC reduction time reduces when the input radiative power is increased and solar-to-fuel conversion efficiency about *6%* at input power of *50 kW*[16].

The reduced level of non-stoichiometry of ceria represented by δ. According to the studies of Panlener et al. [17] and Zinkevich et al. [18], the lowest deviation is about *0.35* in the temperature range of *1000–1500 °C*. Lapp et al. [19] performed an thermodynamic analysis to study the value of non-stoichiometry (δ) at the temperature range of *1000–1500 °C* keeping partial pressure of oxygen from 10^{-2} to 10^{-24} atm. The study of Scheffe and Steinfeld [20] showed that the ceria (CeO_2) requires temperature greater than *1000 °C* to initiate the reduction step. However, the oxygen partial pressure should be less than 10^{-2} bar Bulfin et al. [21] The high temperature (energy input) can be achieved by concentrated solar power (for pilot scale) and by other means such as oxy-fuel radiant heating (for lab scale). The oxygen partial pressure can be controlled by either using a vacuum condition or using an inert gas [22]. The theoretical solar-to-fuel efficiency can be expressed as (Li et al. [23]);

$$\eta_{th} = \frac{n_{fuel} HHV_{fuel}}{Q_{solar}} \tag{4}$$

Solar thermochemical reactors are the most crucial part where the reactions take place and can be categorized as directly and indirectly irradiated reactors. The concentrated solar energy doesn't directly come in contact with reactive materials in indirectly irradiated reactors instead the solar irradiation gets absorbed by opaque wall and gets further transferred through convection and conduction. However, in directly irradiated reactors the concentrated solar energy directly irradiates the reactive materials. The indirectly irradiated reactors are mostly used in solar methane reforming [24–26] as well as in solar thermochemical cycles [27, 28]. They are designed as tubular reactors (single or multi-tube) using alumina material. However, the reactor body material concern cannot be neglected in solar thermochemical cycles as the reduction step takes place at

the temperature higher than *2000* K. Thus the materials having high melting points such as silicon carbide (SiC) and alumina are used in the reactor body. The directly heated reactor possesses the advantage of comparatively efficient heat transfer than an indirectly irradiated reactor because it transfers the energy through radiative heat transfer. The directly-irradiated reactors can be majorly classified into three categories: moving front reactor, packed bed reactor and rotary type reactor. The moving front type reactor has a moving shaft mounted at the reactor center which allows the reaction catalysts to be exposed to the solar radiation directly. They are mostly used with volatile catalysts such as *ZnO/Zn* and SnO_2/SnO thus after the vaporization of some amount of catalysts, freshly coming catalysts remain fully exposed to the solar radiation [29, 30]. The packed bed reactor was firstly used in the year *2012* by Chueh et al. [31] with reticulated porous ceria (*RPC*) foam. In this reactor, the reduction and oxidization reaction can take place continuously alternatively. This cavity-receiver reactor design provides porous surface for effective radiation exposure and can be operated under temperature-swing as well as isothermal condition. In rotary type reactors, the continuous reduction and oxidation take place in two separate regions divided by placing a rotary monolith catalyst axis perpendicular to the reactor axis [10, 32, 33]. Keykhah et al. perfomedthermoeconomic analysis and concluded that the exergy efficiency of the system can be improved from 1% to 3.5% at the expanse of 6$/h increase in the cost [34]. The results of the optical numerical investigation of parabolic trough collectors revealed that the optical efficiency reached about 77.22% [35].

Lougou et al. [36] experimentally and numerically investigated the reactor design and thermochemical energy conversion. Study reported that the targeted radiation receiver surface and the volume of reactor are the main factors which affect the thermochemical energy storage efficiency. Result showed that the reactor efficiency during thermal charging and discharging was reported to be *85.27%* at *1787.73* K and *76.9%* at *1315. 16* K, respectively. In a study carried out by Safari and Dincer [37], two step, three step, four step and hybrid thermochemical water splitting cycles were comparatively evaluated. These thermochemical cycles were evaluated in terms of energy-exergy efficiency and global warming potential (GWP). It was found that the vanadium chlorine yields the highest exergy efficiency of *77%*. Sulfur-Iodine and hybrid sulfur cycles are the most promising candidate having the GWP of *0.48* and *0.50 kg* CO_2*·eq/kg* H_2, respectively. Bhosale et al. [38] performed thermodynamic analysis on SnO_2/SnO water splitting cycle. Results of the study indicated that if the thermal reduction temperature is maintained at *1780* K, the cycle efficiency of *41.17%* and solar-to-fuel energy conversion efficiency of *49.61%* can be achieved. Chen et al. [39] numerically investigated the thermochemical methane dry reforming using foam reactor. The results of the study showed with increasing the velocity and CH_4/CO_2 reduces the methane conversion. However, as the thermal conductivity of solid phase is increased, the methane conversion increases. Study also revealed that the maximum efficiency and conversion is obtained at the porosity and pore diameter of *0.9* and *1.5 mm*, respectively. Wang et al. [40] investigated numerically methane reforming process in porous thermochemical reactor using LTNE model coupled with P1-radiation model. The results of the study indicated that the radiative heat loss poses a strong influence on solid phase temperature, thus it reduces the hydrogen production. Further, as the thermal conductivity of porous media increases, it decreases the temperature of solid phase however, it improves the chemical reaction rate. Wang et al. [41] performed a numerical analysis on methane reforming using LTNE model in a porous media based reactor. The results of the study showed that the fluid phase temperature is affected by the concentrated solar irradiation and forms a big temperature gradient of solid phase. Charvin et al. [42] presented the process analysis of three thermochemical cycles, *ZnO/Zn*, Fe_3O_4/FeO and Fe_2O_3/Fe_3O_4. Study indicated the cost of hydrogen production estimated to be *7.98$/kg* and *14.75$/kg* for *55 MWth* and *11 MWth* solar power plant, respectively. Results also showed that efficiency for Fe_3O_4/FeO, Fe_2O_3/Fe_3O_4 and *ZnO/Zn* reached to *17.4%, 18.6%* and *20.8%,* respectively. Bhosale et al has performed thermodynamic analysis on different cycles to calculate the cycle and solar-to-fuel conversion efficiency on samarium oxide ($\acute{\eta}_{cycle}$=24.4% and $\acute{\eta}_{solar\text{-}to\text{-}fuel}$=29.5%) [43], erbium oxide ($\acute{\eta}_{cycle}$=9.96% and $\acute{\eta}_{solar\text{-}to\text{-}fuel}$=12.01%) [44], Terbium oxide($\acute{\eta}_{cycle}$=39% and $\acute{\eta}_{solar\text{-}to\text{-}fuel}$=47.1%)[45], Zinc oxide-zinc sulfate ($\acute{\eta}_{cycle}$=40.6% and $\acute{\eta}_{solar\text{-}to\text{-}fuel}$=48.9%) [46], Cr2O3/Cr ($\acute{\eta}_{cycle}$=71.1% and $\acute{\eta}_{solar\text{-}to\text{-}fuel}$=54%)[47], MnSO4/MnO ($\acute{\eta}_{solar\text{-}to\text{-}fuel}$=47.6%, 53.1% and 60% with 10, 30 and 50% of heat recovery) using HSC chemistry [48]. The doping effect of metal cations on thermal reduction was analyzed using TGA and results show that at 1400^{0}C, CeZn and CeFe release higher amount of O2 than other $Ce_{0.9}M_{0.1}O_{2-\delta}$ materials [49]. Sarwar et al. [50] experimented and numerically studied the effect of aperture size on efficiency of solar energy harvesting *7 kW* xenon short arc lamp solar simulator. Results indicated that the optimum aperture size is related to irradiance intensity. They also concluded that the power consumption reduces to half with variable aperture size as compared to the fixed temperature. While, variable aperture can maintain the steady temperature of *1000 K, 1100 K* and *1200 K* with *26.8 kW, 33.2 kW* and *26.9 kW*, respectively. Siddiqui et al. [51] proposed a novel solar and geothermal integrated trigeneration system in *CuCl* cycle to generate the electricity, hydrogen and cooling. Results showed the energy and exergy efficiency to be *19.6%* and *19.1%,* respectively. Further, the energy efficiency and exergy efficiency to be *35.3%* and *35.9%,* respectively for hydrogen production in *CuCl* cycle. Jiang et al. [52] investigated the hydrogen production via methane reforming using perovskite

($La_{1-y}CayNi_{0.9}Cu_{0.1}O_3$). Study showed that the increasing calcium substitute increases the perovskite reactivity and methane conversion reaches up to *52%*. It was found that $La_{0.1}Ca_{0.9}Ni_{0.9}Cu_{0.1}O_3$ has the highest reactivity. Sedighi et al. [53] studied the point focus gas phase receiver operated on high temperature. Study concluded that the trend is moving towards the reach of high thermodynamic efficiency thus, the high temperature at outlet will be required in the future. It was also pointed out that the reactor design needs to be improved. Lee et al. [54] carried but a numerical investigation on hydrogen production via methane reforming using a packed bed reactor, sorption reactor and membrane reactor. Results of the numerical investigation showed that H_2 yield rate of *0.00143, 0.00145, 0.00127, 0.00121*, and *0.00852 mol/s* were found with the SEMR with counter-current flow, SEMR with co-current flow, MR with counter-current flow, MR with co-current flow, and a packed-bed reactor, respectively. Wang et al. [55] proposed a new structure for solar receiver/reactor for hydrogen production. They investigated the changing the aperture diameter, width and receiver length. Results showed that the MCR increases when the aperture width is decreased and the maximum porous bed temperature decreases by *17.9* ^0C. It was also found that the reactor performance is improved as the aperture and diameter changes along the flow direction harmoniously.

The solar thermochemical energy storage is high temperature based reversible chemical reactions. It is a two-step process known as charging step and discharging step. In the charging step, the redox material is heated up to *1600* K and in discharging step, $H_2O/CO_2$are converted into fuels at comparatively low temperature [56–59]. Solar thermochemical process is still under development at lab scale and researcher are finding new ways to convert solar thermal energy into clean fuels. The performance of High-temperature thermochemical energy storage system depends upon thermal and chemical characteristics of redox material. Studies have shown that the solar thermochemical process have much potential to become high temperature based energy storage system as compared to other storage technologies [60–65]. Porous media structure has been adopted to increase the thermal performance of the reactor due to the larger area of heat transfer. Banerjee et al. [66] stated that the heat transfer in reactor can be increased by *9* fold by using the RPC rather than bare tubes. A RPC based heat exchanger model was developed and integrated with solar reactor. Study reported the *85-90%* porosity yielded the higher heat transfer and improved solar-to-fuel conversion efficiency [67, 68]. Distribution of solar power density and thermal chemical reaction performance increases with the increasing porosity and cell size also the higher thermal performance leads to higher solar-to-fuel conversion efficiency [69–72]. In another study, it was shown that the use of porous media in thermochemical reactor increases the thermal performance as well as helps in the amalgamation of various redox materials [73, 74]. The coupled conduction-radiation heat transfer in solar reactor to evaluate thermal performance have been explored extensively [75–78]. Many studies have pointed out that the thermal performance of heat storage medium is affected by temperature gradient in porous media in solid phase [79–81]. In past few years, researchers have developed potential candidate redox material to increase the thermal stability and chemical reactivity to increase the solar-to-fuel conversion efficiency [82–86]. Regarding the literature, the reticulated porous ceria (RPC) based solar thermochemical reactors have been considered as better alternative among perspective of industrial applications.

Based on abovementioned studies, as of authors' best of knowledge, effects of RPC thickness and gas flow gap in STCR cavity has not been yet investigated. The present paper aim to investigate following objectives:

1. To investigate the effect of varying RPC thickness on the temperature distribution in porous media as well as in the whole reactor cavity.
2. To study the effect of varying gas flow gap and increasing fluid velocity on the temperature distribution in the porous region along with entire reactor cavity.
3. To explore the geometrical parameters variation effects on flux distribution in the solar thermochemical reactor cavity.

In this work, a numerical analysis (steady-state and transient) has been performed on six hybrids, cylindrical-hemispherical cavity shape models to study the effects of RPC thickness and geometrical parameters of the cavity receiver.

This paper has been structured as: In section-*2*, the adopted methodology including physical model, mathematical modelling, reactor configuration, numerical implementation and mesh independence analysis has been illustrated. Section-*3* discusses the model validation. In section-*4*, the results obtained from the numerical study have been discussed. In section-*4.1*, *4.2, 4.3, 4.4, 4.5*, and *4.6*, the effect of RPC thickness, effect of inert gas flow gap, effect on reactor-receiver, flux distribution, pressure distribution and velocity distribution, respectively have been discussed in detail.

METHODOLOGY

The solar thermochemical production of hydrogen via a two-step water splitting process requires two inputs known as, material input and energy input. In this process, water is used as material input and solar heat is used as the energy input. The solar concentrated energy splits the water into hydrogen and oxygen in a thermochemical reactor at high temperature. The schematic diagram of the solar reactor cavity is shown in Figure 1. This reactor cavity consists of a hybrid, cylindrical and hemispherical reactive chambers. In the solar thermochemical reactor cavity, the RPC region is

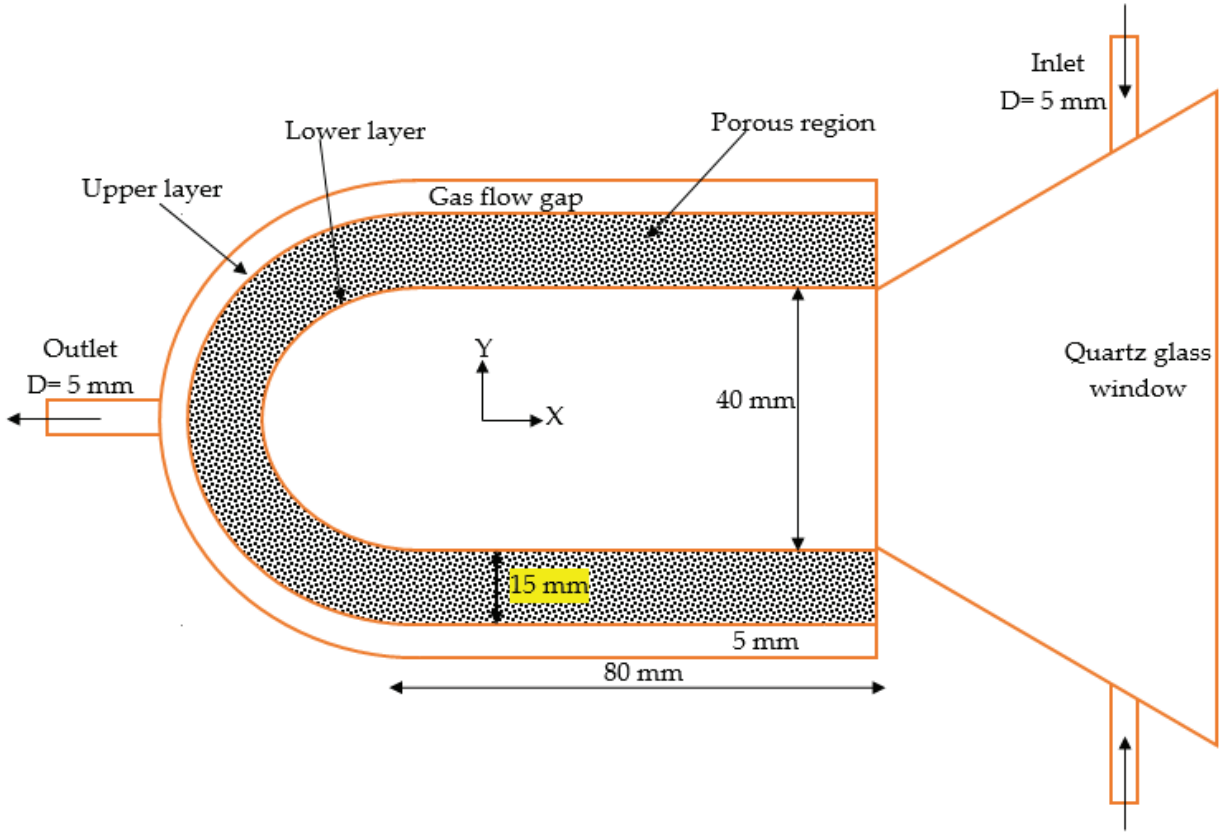

Figure 1. Schematic displaying dimensions of the solar thermochemical reactor-receiver cavity.

the core section having the RPC thickness as *15 mm*, *20 mm* and *25 mm* with *5 mm* and *10 mm* gas flow gap.

In front of the cavity aperture, a transparent quartz glass window is placed which allows the solar radiation to enter the cavity. The solar heat flux on the quartz glass window is applied using a user define functions: UDF heat flux profile in ANSYS fluent version *16.2*. Inlets and outlet are provided in the cavity for the circulation of flowing fluids (nitrogen and argon). As the solar flux radiates the cavity and increases its temperature, the flowing fluid are injected from the inlet, pass through the porous media and exit from the outlet. Flowing fluid allows the temperature to be distributed uniformly in the porous region. The outer region of the cavity is packed in stainless-steel shell and outer layers are made fully insulated to reduce the thermal loss. As some geometric factor affect the thermal performance of the solar thermochemical cavity. In this paper, the effect of RPC thickness and gas flow gap on the thermal performance of reactor cavity has been investigated. The main focus of the study is maintained on the radial and axial heat transfer as well as the distribution of heat flux in the solar thermochemical cavity. In this investigation, entire cavity has been simulated using CFD technique. ANSYS fluent v.*16.2* was used to carry out the simulation.

Physical Models

RPC based solar thermochemical reactor as shown in Figure 1 used for numerical simulation. Solar concentrated radiation enters into the reactor cavity through the transparent quartz glass window and heats the RPC region to enable the redox reactions. The nitrogen gas is fed into the reactor cavity through the inlets to sweep the remains of hydrogen or oxygen from the cavity. Six different reactor cavity models as shown in Figure 2 were considered for the numerical simulation. Figure 2 *(a)*, *(b)*, and *(c)* show the reactor cavities having the RPC thickness as *15 mm, 20 mm*, and *25 mm*, respectively with *5 mm* gas flow gap. Whereas, Figure 2 *(d)*, *(e)*, and *(f)* show the reactor cavities having RPC thickness as *15 mm, 20 mm,* and *25 mm*, respectively but the gas flow gap is increased to *10 mm*.

Mathematical Model/ Governing Equations

The governing equations used in the present simulations are given as follows [87, 88]:

(i) Conservation of mass

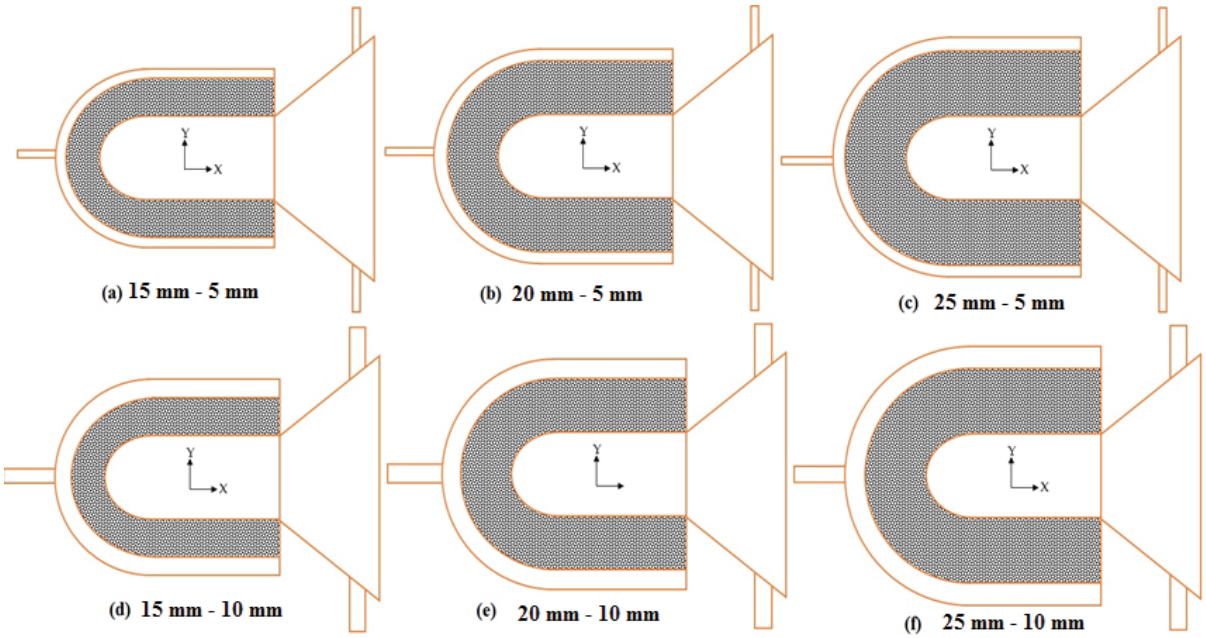

Figure 2. Cases considered in numerical simulation.

$$\textbf{Steady state: } \frac{\partial \rho}{\partial t} + \nabla.\left(\rho_f v\right) = 0 \quad (5)$$

However, when the mass transfer occurs in the RPC domain the mass conservation equation of non-reactive RPCare given below:

Mass transfer

$$\frac{\partial(\rho_f Y_i)}{\partial t} + \nabla.(\rho_f v Y_i) = 0 \quad (6)$$

$$\frac{\partial(\chi\rho_f Y_{O_2})}{\partial t} + \nabla.(\chi\rho_f v Y_{O_2}) = S_{m,O_2} \quad (7)$$

$$\frac{dm_p}{dt} = \dot{m}_p \quad (8)$$

The absolute value of particle mass transfer rate equals the rate of oxygen evolution. The particle mass changed fraction defines the reaction rate as shown [89];

$$\frac{dx}{dt} = k_{red}(1-x) \quad (9)$$

$$x = \frac{m - m_i}{m_f - m_i} \quad (10)$$

In the above given equations, k_{red} is the reduction rate co-efficient and m, mi and m_f denote the time-dependent, initial and final mass of the particle and the value of m can be calculated by the Eq. (11)

$$m = m_i - \delta n_{CeO_2} \frac{M_{O_2}}{2} \quad (11)$$

Thus, the reaction rate can be given as Eq. (12)

$$\frac{dm_p}{dt} = (m_f - m_i)k_{red}\left(1 + \frac{\delta \frac{m_i}{M_{CeO_2}} M_{O_2}}{2(m_f - m_i)}\right) \quad (12)$$

$$\frac{\delta}{(0.35-\delta)} = 8700\left(P_{O_2} bar\right)^{-0.217} \exp\left(-195.6\ kJ-mol^{-1}/RT\right) \quad (13)$$

In the above given equation, δ denotes the non-stoichiometric coefficient and it depends on the reaction temperature as well as the oxygen partial pressure [21]. The oxygen partial pressure can be calculated from the Eq. (14);

$$P_{O_2} = (M_{O_2} \times P_{tot}) \quad (14)$$

(ii) Conservation of momentum

The momentum conservation equation in the porous media based STCR is solved as

$$\frac{\partial}{\partial t}\left(\rho \vec{v}\right)+\nabla.\left(\rho \vec{v}\vec{v}\right)=-\nabla p+\nabla.\left(\mu\nabla \vec{v}\right)+S_p \quad (15)$$

The fluid pressure drop source term (S_p) is calculated as [90]:

$$S_p=-\left(\frac{1039-1002\phi}{d_s^{\,2}}\right)\mu u-\left(\frac{0.5138\phi^{-5.739}}{d_s^{\,2}}\right)\rho_f u^2;\quad 0.66\le\phi\le 0.93 \quad (16)$$

The flow is given at fluid inlet in the porous media, the gradient is set *0* at the fluid outlet.

Inlet: $u = u_0$, $v = 0$

Outlet: $\dfrac{\partial u}{\partial x}=\dfrac{\partial u}{\partial y}=\dfrac{\partial v}{\partial x}=\dfrac{\partial u}{\partial y}=0$

(iii) Conservation of energy

$$\frac{\partial}{\partial t}(\rho h-p)+\nabla.\left[\vec{v}\left(\rho h\right)\right]=\nabla.(\lambda_{eff,f}\nabla T)+S_h \quad (17)$$

$$S_h=h_v(T_s-T_f) \quad (18)$$

Where h_v (W/m^3k) is known as volumetric convection heat transfer coefficient and it can be calculated using the correlation given by Wu et al. [90]

$$h_v=\frac{\lambda_f\left(32.504\phi^{0.38}-109.94\phi^{1.38}+166.65\phi^{2.38}-86.98\phi^{3.38}\right)\mathrm{Re}^{0.438}}{d_s^{\,2}};\quad (0.66\le\phi\le 0.93\ and\ 70\le \mathrm{Re}\le 800) \quad (19)$$

For solid zones, the Eq. (19) becomes,

$$\frac{\partial}{\partial t}(\rho h)=\nabla.(\lambda_{eff,s}\nabla T)+S_s \quad \textbf{(20)}$$

$\lambda_{eff,f}$ and $\lambda_{eff,s}$ denote the effective thermal conductivity of the fluid and solid phase, respectively. These entities can be calculated using the following given correlations [91];

$$\lambda_{eff,f}=\phi\lambda_f \quad (21)$$

$$\lambda_{eff,s}=\lambda_s(1-\phi) \quad (22)$$

The source term includes the radiative (S_{rad}), convective ($S_{conv,s}$) as well as heat dissipation (S_w).

$$S_s=S_{conv,s}+S_{rad}+S_w \quad (23)$$

- Convective heat transfer source term:

The convective heat transfer source term calculates the heat transfer between solid and fluid phase.

$$S_{conv,s}=-S_{conv,f}=-h_v(T_s-T_f) \quad (24)$$

- Wall heat dissipation source term:

Solar thermochemical reactor operates at high temperature thus the heat dissipation consideration becomes crucial and it can be calculated by following equation,

$$S_w=-\varepsilon_w\sigma(T_s^{\,4}-T_0^{\,4}) \quad (25)$$

(iv) Radiative transfer equation

The solution of radiative transfer equation (RTE) [92] gives the irradiative source term mentioned in Eq. (15)

$$\frac{dI(s)}{ds}=-k_eI(s)+k_aI_b(s)+\frac{k_s}{4\pi}\int_{4\pi}I(s,\vec{\Omega}')\phi(\vec{\Omega}',\vec{\Omega})d\Omega' \quad \textbf{(26)}$$

In the equation given above, I denotes the local radiation intensity in the porous medium and ke is known as the extinction coefficient [93]. The absorption and scattering coefficient can be calculated using correlations given below [91];

$$k_a=\frac{3\varepsilon(1-\phi)}{2d_s} \quad (27)$$

$$k_s=\frac{3(2-\varepsilon)(1-\phi)}{2d_s} \quad (28)$$

$$k_e=k_a+k_s=\frac{3(1-\phi)}{d_s} \quad (29)$$

Discrete Ordinates Irradiative Transfer Model

The energy and radiative transfer equation for fluid flow through the porous media can be written as follow [94];

Fluid energy equation:

$$-\varphi\rho_f u_f c_f\frac{\partial T_f}{\partial x}-(1-\varphi)hA(T_f-T_s)+\varphi Q(y)\delta(x)+\varphi k_f\left(\frac{\partial^2T_f}{\partial x^2}+\frac{\partial^2T_f}{\partial y^2}\right)=0 \quad (30)$$

Solid energy equation:

$$\nabla.q+(1-\varphi)hA(T_s-T_f)-(1-\varphi)k_s\left(\frac{\partial^2T_s}{\partial x^2}+\frac{\partial^2T_s}{\partial y^2}\right)=0 \quad (31)$$

In the above given equations, h is the heat transfer coefficient and A is the surface area of the porous medium. The thermal conduction via. gas can be easily neglected due to the poor thermal conductivity of the inert gas. In discrete ordinates (*DO*) radiation model, the radiative transfer equation (RTE) are solved for finite number of discrete solid angles. Each angle is in association with directional vector (*s*). The number of transport equation solved by *DO* model are equal to the directions (*s*).

Thermophysical Parameters

The Thermophysical properties used in the numerical analysis are given in Table 1.

Reactor Configuration and Modeling

The effects of RPC thickness and gas flow gap variation on the thermal and fluid flow characteristics in the solar thermochemical reactor cavity were studied. The configurations for six STCR cavity models has been presented in Table 2. The initial and boundary conditions adopted in the simulation are listed in Table 3. The RPC zone consists of RPC with varying thickness (*15-25 mm*) as well as the gas flow gap (*5-10 mm*). The inlet velocities were calculated in Reynolds number range of *100-300*. The non-uniform flux profile was applied to the quartz glass window to generate the uniform temperature in the porous region of the reactor cavity. The outermost surface of the reactor cavity was made fully insulated to reduce the thermal loss.

Numerical Implementation

To carry out the numerical simulation, the solar collector was simulated using an open source software, SolTrace, which traces the solar ray path by MCRT technique. MCRT uniformly distributes solar power by dividing it into larger number of rays determined by the sun shape and slope error [98, 99]. The interaction between the rays and the reactor cavity is influenced by the transmissivity, reflectivity and absorptivity. The flux profile obtained from the

Table 1. Thermophysical properties [71]

CeO_2–RPC	*Value/Correlation*	*T (K)*
Density (*kg/m³*)	*7220*	-
Porosity (*%*)	*63*	-
Total CeO_2 mass (g) [95]	*1413*	-
Permeability (*m²*) [96]	$(4.63376)\times10^{-8}$	-
Thermal conductivity solid (*W/m-K*) [96], [97]	$\left[\frac{\left(17.8004-0.02402\times T+0.0000112032\times T^2-1.7\times10^{-9}\times T^3\right)}{\left(7.9799+0.00483384\times T-9.3397\times10^{-6}\times T^2+2.8\times10^{-9}\times T^3\right)}\right]$	*280 –2000*
	0.4	*> 2000*
Specific heat capacity *(J/kg-K)*	$299.8695684 + 0.2697656\times T-0.0001271\times T^2$	*280 – 1100*
	444.27	*> 1000*
Surface reflectance *(at δ = 0.035)*	$0.2866-3\times10^{-5}\times T$	*300-2500*
Absorption coefficient $CeO_{1.965}$ *(1/m)*	$\left(1-\left(-0.00006\times T+0.411\right)\right)\times497.8$	*300-2500*
Scattering coefficient $CeO_{1.965}$ *(1/m)*	$\left(-0.00006\times T+0.411\right)\times497.8$	*300-2500*
Fluid-solid heat transfer coefficient *(W/m²-K)*	*10000*	-
Fluid-solid area density *(1/m)*	*952*	-

Table 2. Reactor cavity models configuration

Part name	**Case-1 Dimensions (mm)**	**Case -2 Dimensions (mm)**	**Case -3 Dimensions (mm)**	**Case -4 Dimensions (mm)**	**Case -5 Dimensions (mm)**	**Case -6 Dimensions (mm)**
Cylindrical Length	*80*	*80*	*80*	*80*	*80*	*80*
Hemispherical inner radius	*20*	*20*	*20*	*20*	*20*	*20*
RPC thickness	*15*	*20*	*25*	*15*	*20*	*25*
H_2/O_2 flow gap	*5*	*5*	*5*	*10*	*10*	*10*
Inlet diameter	*5*	*5*	*5*	*10*	*10*	*10*
Outlet diameter	*5*	*5*	*5*	*10*	*10*	*10*
Total length of cavity	*120*	*125*	*130*	*125*	*130*	*135*

Table 3. Boundaryconditions

Surface	*Boundary conditions*
Inlets	$v_{inlet} = \frac{\overset{*}{v}}{Ac_{inlet}}$; $T_{inlet} = T_{initial}$; $n_{N_2} : n_{O_2} = 1:10^{-5}$
Outlet	$P_{out} = P_{atm}$
Inner surface	$k_q \frac{\partial T}{\partial n} = S_{E,rad} + h_q \Delta T$; $\varepsilon = 0.08,\ \tau = 0.86$
Insulation wall	$k_s \frac{\partial T}{\partial n} = \Delta q_r + h_s \Delta T$; $\varepsilon = 0.28,\ \tau = 0$
Quartz window	$T_{aperture} = T_{initial}$; $\varepsilon = 0.08,\ \tau = 0.86$
Other surfaces	$\frac{\partial T}{\partial n} = 0$

Table 4. Initial conditions

Preheating stage	
$T_{initial}$	*300 K*
Pressure	*1 atm*
Species mole ratio	N_2:O_2::*1:0*
Ceria reduction stage	
$T_{initial}$	*1300 K*
Species mole ratio	N_2:O_2::*1:1e-5*
Rate of reaction	*0*

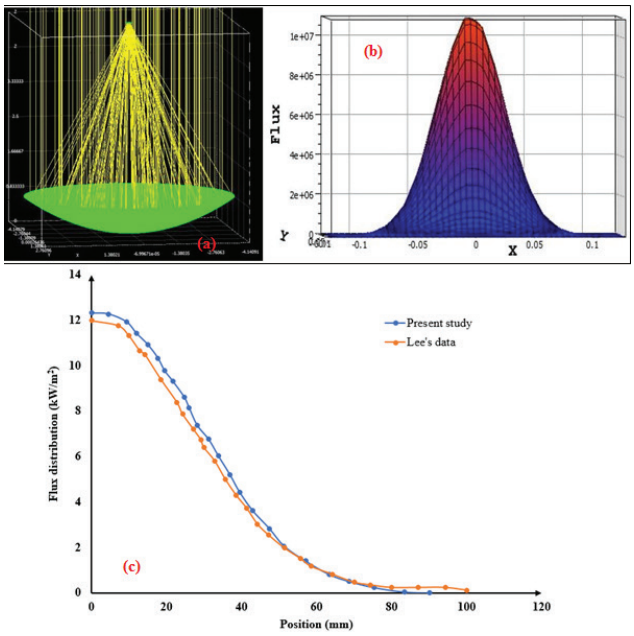

Figure 3. Solar heat flux profile and MCRT validationwith Lee[100].

SolTrace shown in *Figure 3* was validated against Lee's study and further used as radiative flux boundary condition on the quartz glass window.

ANSYS Fluent v.16.2 solver was used to solve the conservation equations by the finite volume method with a tetragonal/hexagonal unstructured mesh having *0.5 mm* element size. The DO radiation model was applied to calculate the radiation heat transfer (RTE equation) in the solar thermochemical reactor cavity. Steady-state simulation with SIMPLE first-order upwind for discrete ordinates and second order for energy calculation was implemented. The transient simulation for cavity preheating as well as CeO_2 reduction was carried out using first order implicit unsteady scheme having a time step of *0.2* second. The non-stoichiometric CeO_2 reduction was modelled by species transfer at porous wall surface to solve the mass transfer equations.

MODEL VALIDATIONAND MESH INDEPENDENCE ANALYSIS

The quality of the mesh is one of the crucial factors which affects the numerical results. Thus, it becomes necessary to adopt adequate mesh for the numerical simulations to obtain precise results. To carry out mesh independence analysis, nine mesh sizes were compared. The plot in the Figure 4(a) shows that as the number of elements increases, the temperature of the reactor cavity reduces and provides results with accuracy. Finally, the temperature deviation reduces to a minimum between element sizes *0.3 mm* to *0.2 mm*. Thus, *0.3 mm* mesh element size with *83102* elements was adopted in this numerical study.

The study available by Zhang et al. [101] is used to validate the numerical model adopted in this paper. P1 approximation radiation model with similar operating and boundary conditions were used in a SiC porous media based reactor cavity with porosity of *0.8*, the emissivity of *0.92*, and mean cell size *1.5 mm*. The density, thermal conductivity, and heat capacity of porous SiC were considered as *3200 kg/m³*, *80 W/(m²-K)*, and *750 J/(kg-K)*, respectively. The total depth of the cavity and the porous medium was taken as *130 mm* and *60 mm*, respectively. Air was considered as flowing fluid inside the cavity. The velocity of flowing fluid was taken as *0.005m/s* and the inlet temperature was considered to be *300 K*. The fluid phase temperature distribution along the centerline of the solar thermochemical reactor was compared with the referred study. *Figure 4(b)*shows good agreement between the fluid phase temperatures of both simulations. Hence present numerical scheme is used for analysis.

The thermodynamic and Ceria reduction models were simulated and validated against the experimental results of non-stoichiometric coefficient with bulfin et al. [21]. The reduction reaction of ceria pellet with *65%* void fraction subjected to *100W* radiative power was modelled.The results of CeO_2 non-stoichiometric coefficient between the present numerical study and the experimental data as

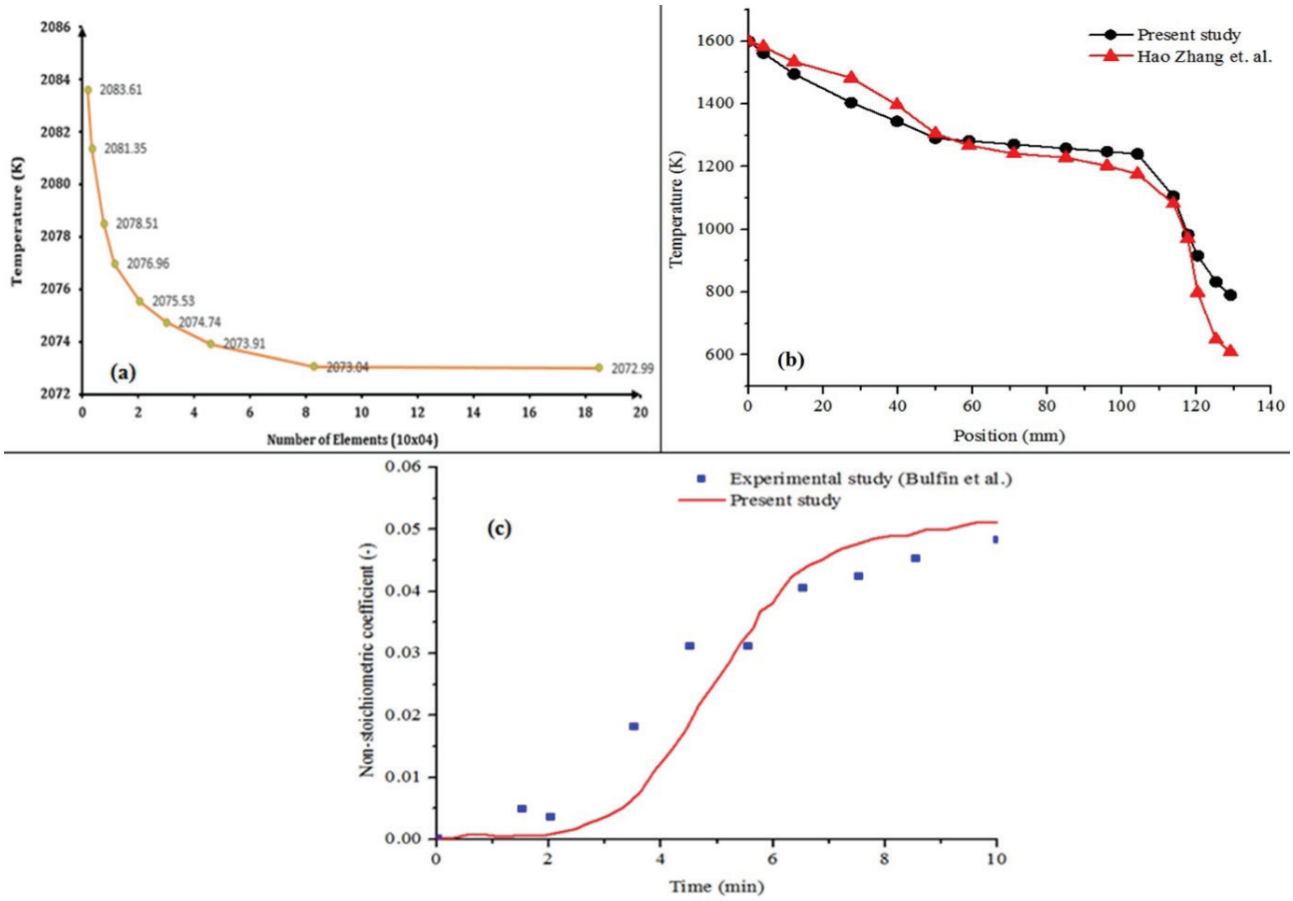

Figure 4. (a) Grid (mesh) independence analysis, (b) Fluid phase temperature distribution along the centerline of solar thermochemical reactor compared with Zhang et. al. [101], (c) Non-stoichiometric coefficient (δ) against time validated with Bulfin et al. [21].

shown in the Figure 4 (c). The minor differences in the comparable results are caused by the operating conditions and simulation assumptions.

RESULTS AND DISCUSSIONS

RPC Thickness

The RPC thickness of the reactor cavity was varied to study its effects on solar flux distribution and temperature distribution in porous media. Figure 7 shows the temperature contours for RPC thickness of *15 to 25 mm* with *5 mm* gas flow gap. It can be seen for 15 *mm* RPC thickness, argon and nitrogen gases generate uniform temperature distribution for Reynolds number *100*. However, as the value of Reynolds number increases to *300*, the cavity temperature reduces. Similar temperature distribution can be seen for *20 mm* and *25 mm* RPC thickness. Figure 5 shows the temperature contours for RPC thickness of *15, 20* and *25 mm* with *10 mm* gas flow gap. It can be seen that when the gas flow gap is increases, the fluid velocity decreases and fluid spends rather more time in the cavity before it exits through the outlet as compared to the *5 mm* gas flow gap.

Temperature distribution in the radial direction

The non-uniform radiation heat flux profile was applied at the front transparent quartz glass window. As the flux enters the reactor cavity, it heats the cavity and generates the temperature distribution in the radial as well as in the axial direction in the porous RPC region. The analysis of temperature distribution in the radial direction in porous media having different thickness (*15 mm, 20 mm*&*25 mm*) are studied which allows better understanding of the optimum required thickness of the porous region in the solar thermochemical cavity. Figure 6(a) show the radial temperature distribution in porous media for *25 mm* RPC thickness with *5 mm* and *10 mm* gas flow gap, respectively. The temperature in the RPC region with *5 mm* flow gap is uniformly distributed for both flowing fluids. However, the increasing value of the Reynolds number affects the temperature distribution. The upper layer temperature of porous media goes up to *1580.91 K* and *1509.94 K* for argon

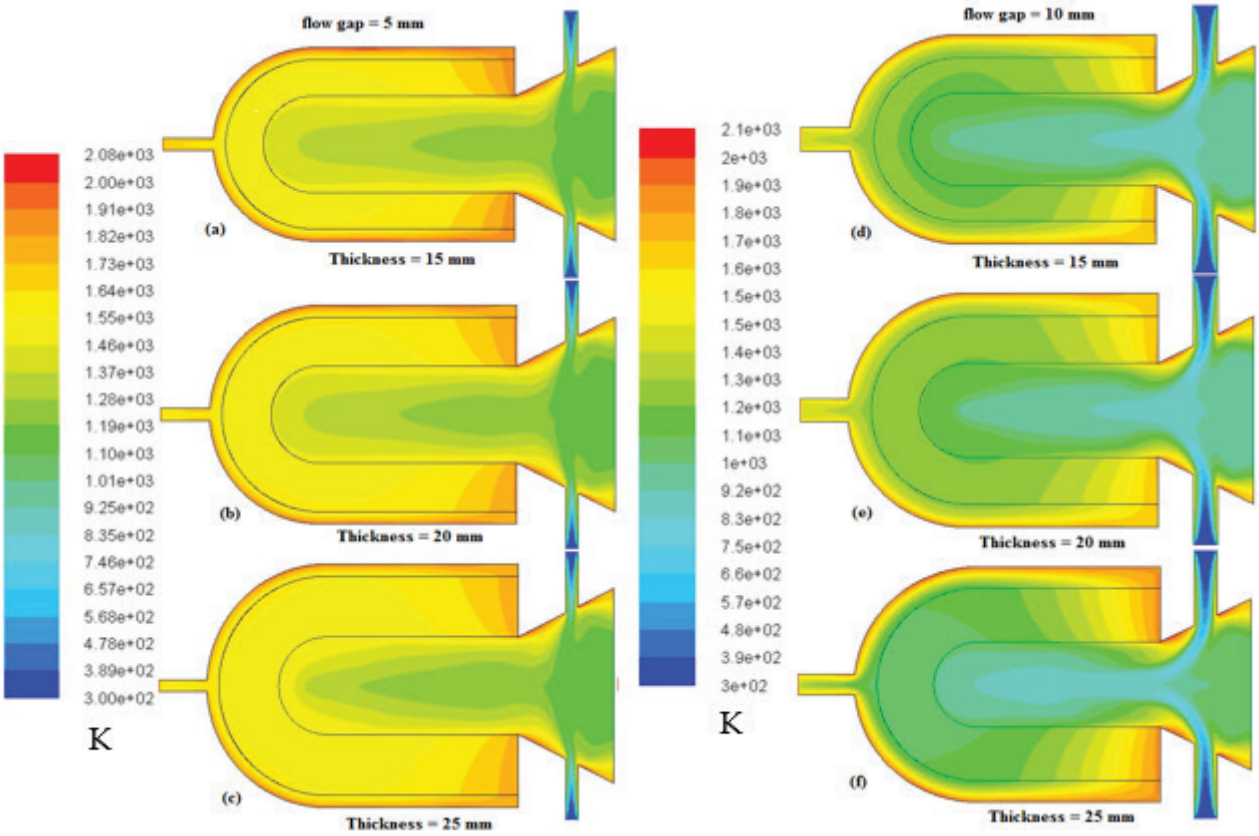

Figure 5. Temperature (K) contours of 15 mm, 20 and 25 RPC thickness with 5 mm and 10 mm inert gas (N_2) flow gap.

and nitrogen, respectively. The avg. temperature of porous media for argon and nitrogen is recorded to be *1549.08 K* and *1463.38 K*, respectively. The increasing thickness of the gas flow gap from *5 mm* to *10 mm* substantially decreases the porous media temperature in the radial direction as shown in the *Figure 6 (b)*. The avg. temperature of the porous media drops by *270.3* K and *304.35* K and it suggests that in any case argon is better choice as inert gas in STCR cavity to maintain higher temperature.

Temperature distribution in the axial direction

The analysis of temperature distribution in the axial direction in porous media is necessary to have a better understanding of the optimum required length of the RPC region in the solar thermochemical cavity. The temperature distribution in the axial direction in the porous media for *15 mm* RPC thickness with *5 mm* and *10 mm* gas flow gap for two flowing fluids, nitrogen and argon has been shown in Figure 6 (c) & (d).

The radiative flux generates the uniform temperature distribution over the porous media length of *80 mm*. The combination of *5 mm* flow gap and Ar gas makes the perfect combination to achieve the required high temperature in the porous media to initiate the redox reactions. The average temperature of porous media is decreased by *50.98* K for nitrogen as compared to argonat *Re=100*.

Effect of Gas Flow Gap

The gas flow gap prolongs the gas and reactant (RPC) contact time and path in the preheating stage. Thus, it becomes crucial to analyze the influences of gas flow gap in the STCR cavity. The radial temperature distribution in the gas flow gap of *5 mm* and *10 mm* has been plotted in the Figure 7 (a)&(b), respectively. In the gas flow region, argon and nitrogen both achieve almost same temperature and also it has been seen that the *5 mm* gas flow gap is more suitable option as it offers low temperature gradient in the radial direction as compared to *10 mm* flow gap. As fluid comes down through the inlet and moves through the porous media, it creates a vortex along the porous media and gas flow gap contact region. As the gas flow gas is increased from *5 mm* to *10 mm*, the effect of vortex gets subdued. Increasing velocity in the gas flow gap and the RPC region leads to vortex formation. Narrow gas flow gap increases the velocity and since the RPC thickness remains content, the fluid hits the insulation walls and alters the velocity vector direction. It is clearly evident that as the gas flow gap increases with constant RPC thickness, the average temperature decreases.

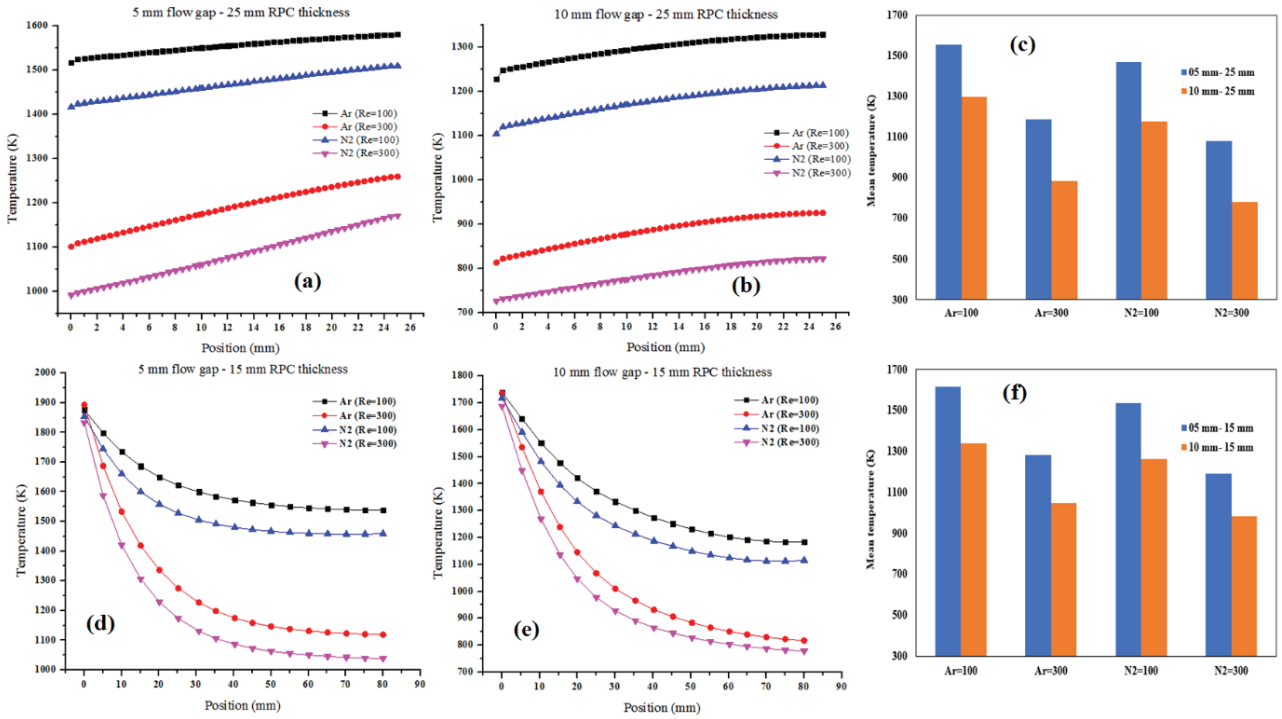

Figure 6. Temperature plot for (a) 25 mm RPC thickness – 5 mm flow gap; (b) 25 mm RPC thickness – 10 mm flow gap in radial direction; (c) Bar graph showing the mean temperatures in radial direction of porous media; & (d) 15 mm RPC thickness – 5 mm flow gap; (e) 15 mm RPC thickness – 10 mm flow gap in axial direction; (f) Bar graph showing the mean temperatures in axial direction of porous media.

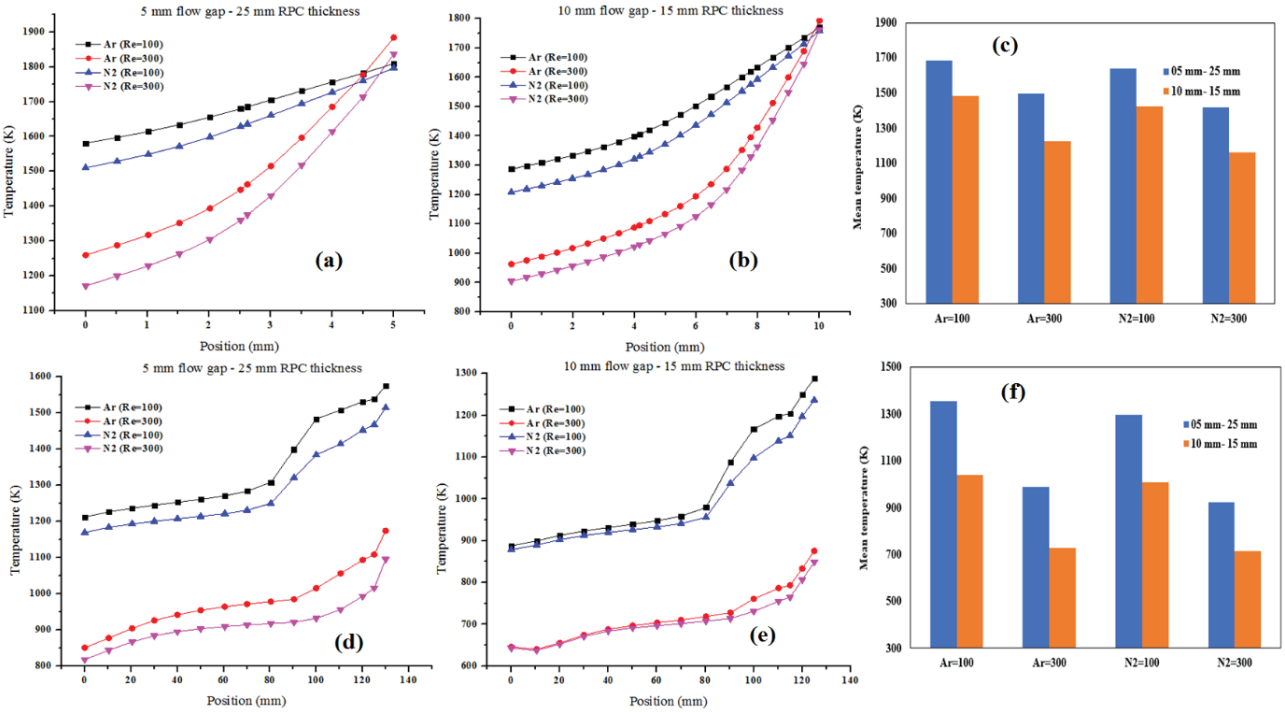

Figure 7. Temperature plot for (a) 5 mm flow gap; (b) 10 mm flow gap; (c) Bar graph showing the mean temperature for 5 mm and 10 mm gas flow gap;& (d)Reactor temperatures for 15 mm RPC thickness –5 mm flow gap; (e) 15 mm RPC thickness –10 mm flow gap along the centerline; (f) Bar graph showing the mean temperatures for 5 mm and 10 mm gas flow gap with 25 mm and 15 mm RPC thickness, respectively.

Reactor Temperature Distribution

The analysis of temperature distribution in the solar thermochemical reactor cavity is necessary to have a better understanding of the optimum required length of the cavity receiver to carry out the solar thermochemical water splitting process efficiently. The temperature distribution in the STCR cavity along the centerline for *25 mm* RPC thickness with*5 mm* gas flow gap and *15 mm* RPC thickness with *10 mm* gas flowcase have been shown in Figure 7(c)&(d), respectively.The temperature for both flowing fluids is uniformly distributed over the entire length of the cavity. However, as the velocity increases, the average temperature of the porous media decreases but the average temperature for argon for all cases remains higher compared to nitrogen due to strong cooling effect of nitrogen. The increasing thickness of RPC zone combined with content gas flow gap leads to decrease in the average fluid temperature in the STCR cavity along the centerline. From the temperature distribution in steady state and transient analysis in the STCR cavity, it is evident that argon achieves slightly higher temperature as compared to nitrogen in STCR cavity as well as in the porous region. However, when reduction cycle completes and oxidation cycle starts, temperature needs to be reduced and nitrogen works as a controlling factor due to its cooling capacity. Thus, nitrogen gas proves itself a quite suitable candidate as sweep gas.

Flux Distribution

The solar flux profile is applied to the transparent front quartz window. The solar flux enters into the cavity and heats the entire reactor cavity including flowing fluid and cavity walls from inside.Solar flux distributioninside the solar thermochemical cavity for *15 mm, 20 mm* and *25 mm* RPC thickness has been shown Figure 8. The solar flux distribution is uniformly distributed in the STCR cavity and it shows higher magnitude at the front quartz window side and lowest at the outlet side. The flux distribution is highly affected by the cooling effect of the flowing fluid and fluid velocity. The highest magnitude is seen in the cavity with *15 mm* RPC thickness and lowest in the cavity with *25 mm* RPC thickness.

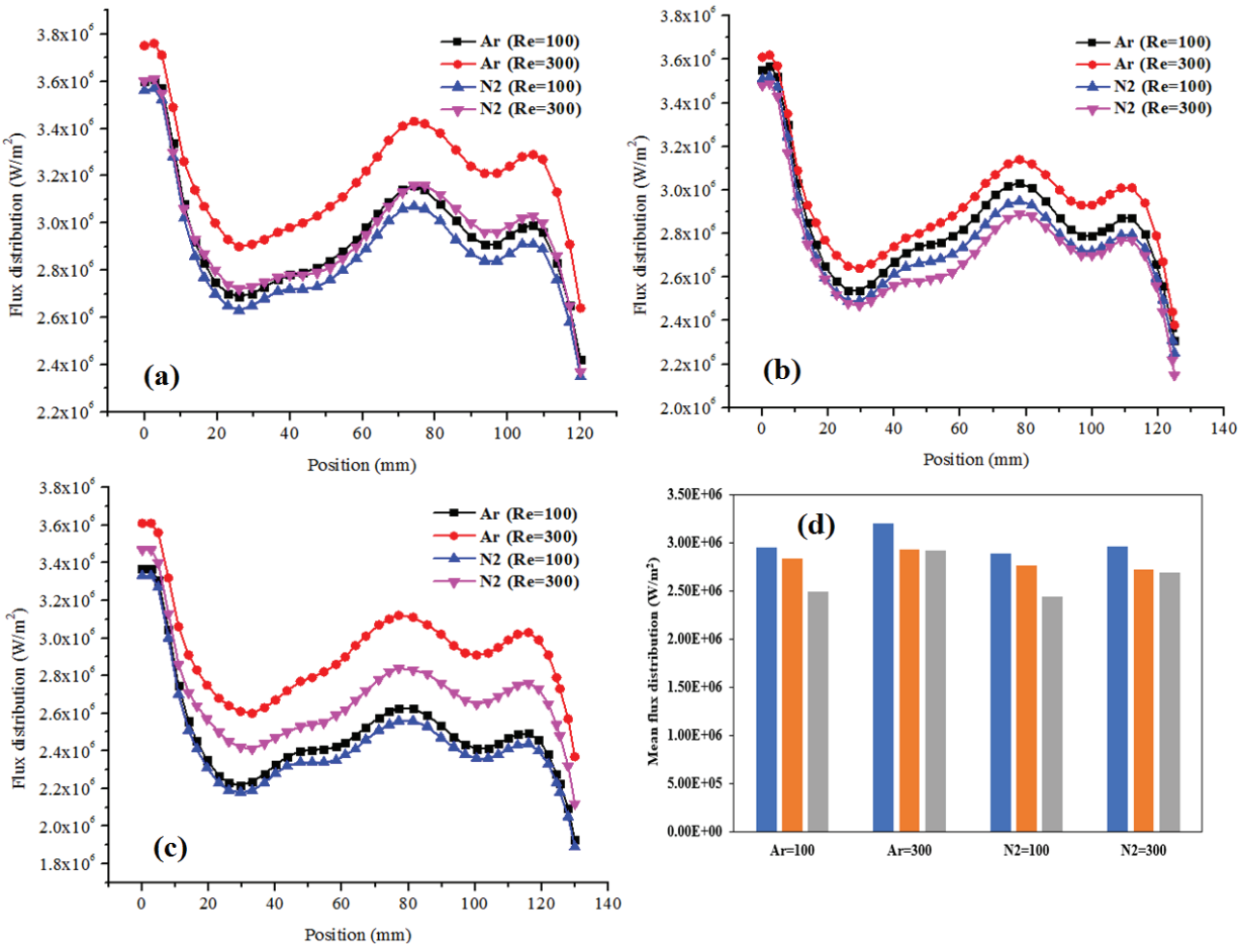

Figure 8. Flux distribution in the solar thermochemical cavity; (a) RPC thickness 15 mm(b) RPC thickness 20 mm (c) RPC thickness 25 mm with 5 mm flow gap.

TRANSIENT ANALYSIS

Solar thermochemical water splitting is a time bound chemical process which occurs in two subsequent steps. To simulate the first *i.e.* reduction step of ceria based solar thermochemical cycle for chemical reaction analysis, transient study was also carried out. This step was subsequently divided into two part were in the first part the STCR cavity was first preheated for the period of two minutes to evaluate the rise in temperature and in the second part, the ceria reduction reaction was initiated and carried out for *10* minutes while subjecting the RPC medium at the initial temperature of *1280* K.

Preheating Stage

Since the reduction of ceria is high temperature based reaction thus, preheating allows the cavity to reach at a temperature where the reduction takes without further delay. The radiative flux is uniformly distributed in the interface regions and in the porous domain. Since the volume of the STCR cavity remains constrained, there is a commutation between cavity and the reactive RPC region. There RPC thickness (*15 mm, 20 mm*, and *25 mm*) has been studied and the velocity profiles has been shown in Figure 9 (1). The larger cavity space improves the velocity distribution and gas velocity reaches to a relative uniform value before entering the porous region. The vortex gets formed in the

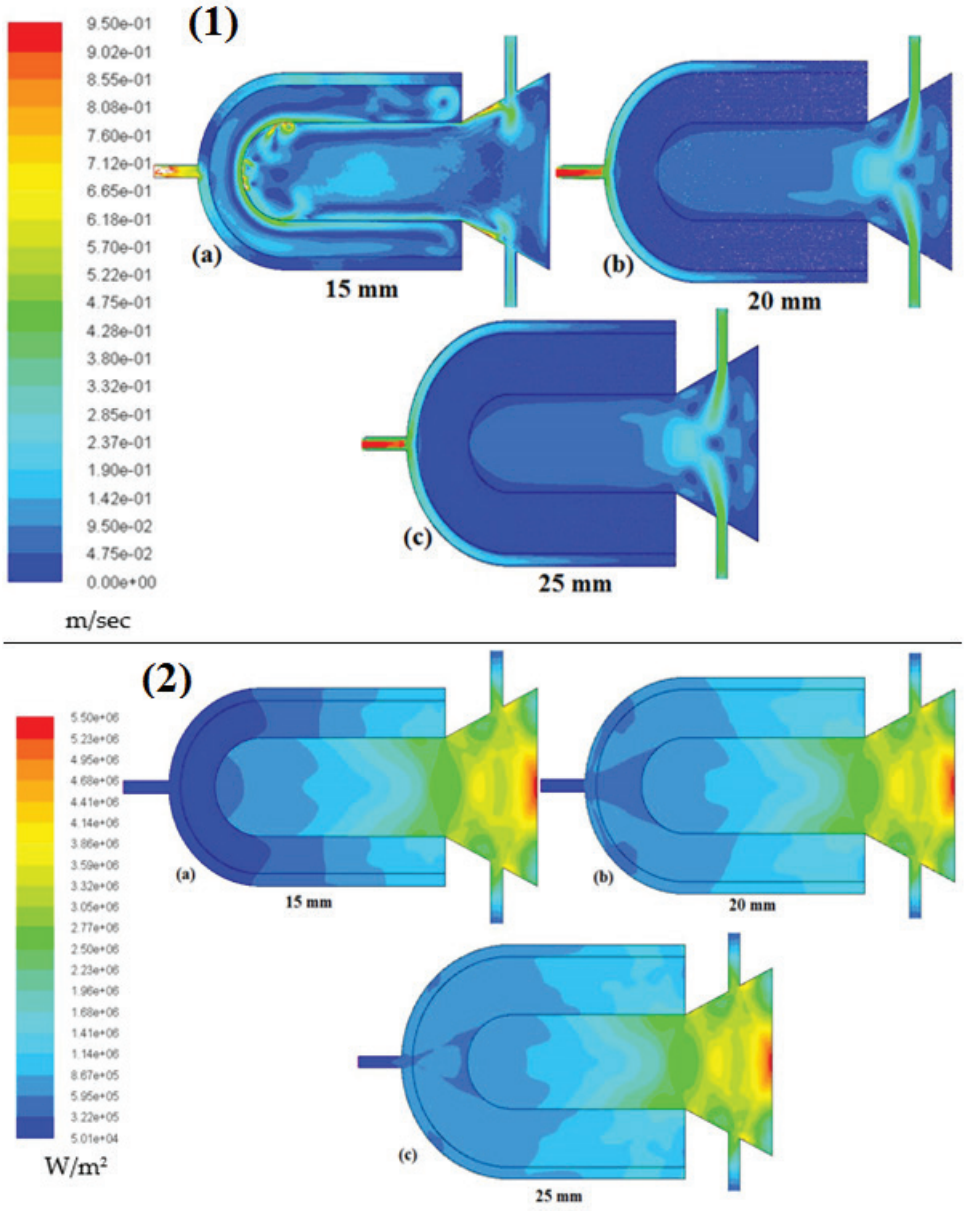

Figure 9. (1) Time dependent velocity distribution & (2) Time dependent incident irradiation contours at 120 sec.

smaller RPC thickness (*15 mm*) cavity which forms a dead zone close to the porous region interface as seen from the velocity contours. The dead zone doesn't allow efficient heat transfer as well as the reaction mechanism in the reactive RPC region. However, this conditions seen to be improved significantly in the *25 mm* RPC thickness cavity.

The variation in RPC thickness plays a crucial role in achieving the uniform flux distribution in the STCR cavity. Moreover, thermofluidic characteristics are also influenced by the RPC thickness which allow to attain required operational temperature to carry out redox reactions. The contours for incident radiation for all three cases at *120 sec* has been shown in the Figure 9 (2). TheSTCR cavity with *15 mm* RPC thickness attains the lowest radiant flux whereas 25 mm RPC thickness cavity attains the highest magnitude radiant flux at the same power. Given the operating CDF algorithm for DO model, the incident radiation takes account of the receiving radiation for each cell which can be seen in the flux distribution contours. The aperture of all three cavities are same (*40 mm*) thus radial radiative transfer path for incident radiation becomes the strongest factor to influence the uniform flux distribution in the cavity porous region. The STCR cavity with *25 mm* RPC thickness has the longest radial path which allows the development and uniform distribution of radiation flux as shown in Figure 9(2)-(c).

The temperature contours considering the conjugate heat transfer at *120 sec* has been shown in Figure 10 (1).The higher temperature in the STCR cavity with *15 mm* RPC region is due to the higher incident irradiation distribution. Even though, the temperature is also higher in *20 mm* and *25 mm* thick RPC cavity but the incident irradiation distribution is not consistent which directly affects the temperature distribution in the whole cavity. This phenomenon can be explained as the opposite influences of radiation and convention heat transfer in porous region. The strong heat convection between the incoming cold fluid and porous interface leads to temperature drop due to dominating heat convection where all the accumulated energy in the porous region is transferred to the cold fluid which results in low temperature in the RPC zone.Time dependent temperature profiles for all three RPC thickness has been shown in Figure 10 (2). The fluid phase temperatures of *15 mm* and *25 mm* RPC thickness attains the highest and the lowest temperature, respectively in *120 sec*. However, it was seen that the *15 mm* RPC zone shows comparatively more variation in fluid phase due to convection effects. In each case, the temperature profiles are consistent with incident radiation flux.

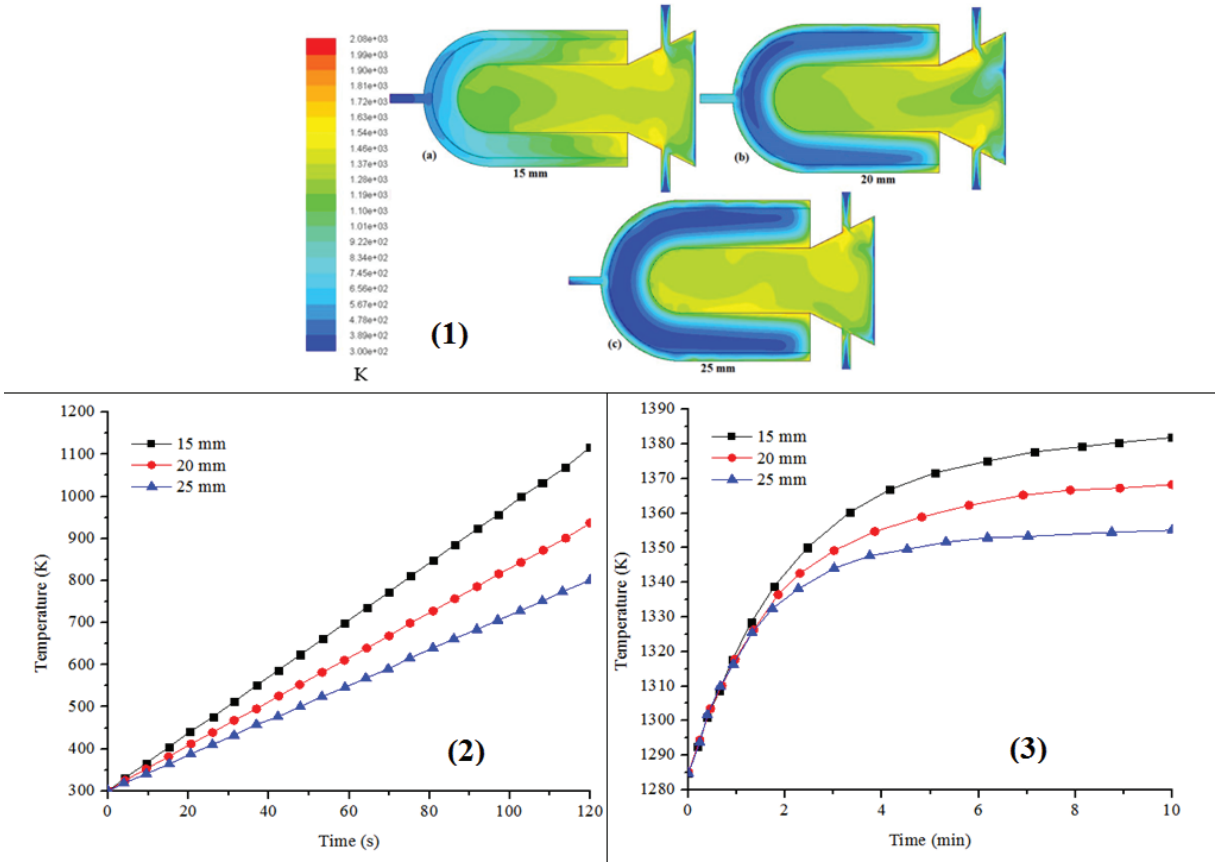

Figure 10. (1) Time dependent temperature contours at *120 sec;* (2) Time dependent temperature distribution for different RPC thickness at *120 sec*&(3) Time dependent fluid phase temperature of porous media during reduction reaction at 10 mins.

Reduction Stage

The reduction reaction step was initiated for H_2O dissociation which gives the oxygen evolution. Firstly, the thermodynamic analysis was carried out using HSC chemistry software. As results show in Figure 11 (a) that ΔG (gibbs free energy) increases with the increasing temperature in reduction reaction of ceria. For instance, in ceria reduction rection ΔG increasees from 140.70 kcal to 295.167 kcal at the temperature increase of 773 K to 1773 K. The vapor pressure in the thermal reduction reaction of ceria is plotted in the Figure 11 (b). It was indicated that the reduction temperature has strong influence on the vapor pressure as it reduces at first with increasing temperature till 1273 K and reduces afterwards.

The CeO_2 reduction reaction is thermodynamically analyzed to be initiated at above *1200* K. Thus, the reduction reaction was carried out for *10 mins* under SolTrace generated solar flux profile as shown in Figure 3(a). Since, the rate of reaction is the function of temperature, the time dependent fluid phase temperature of porous media at *10*

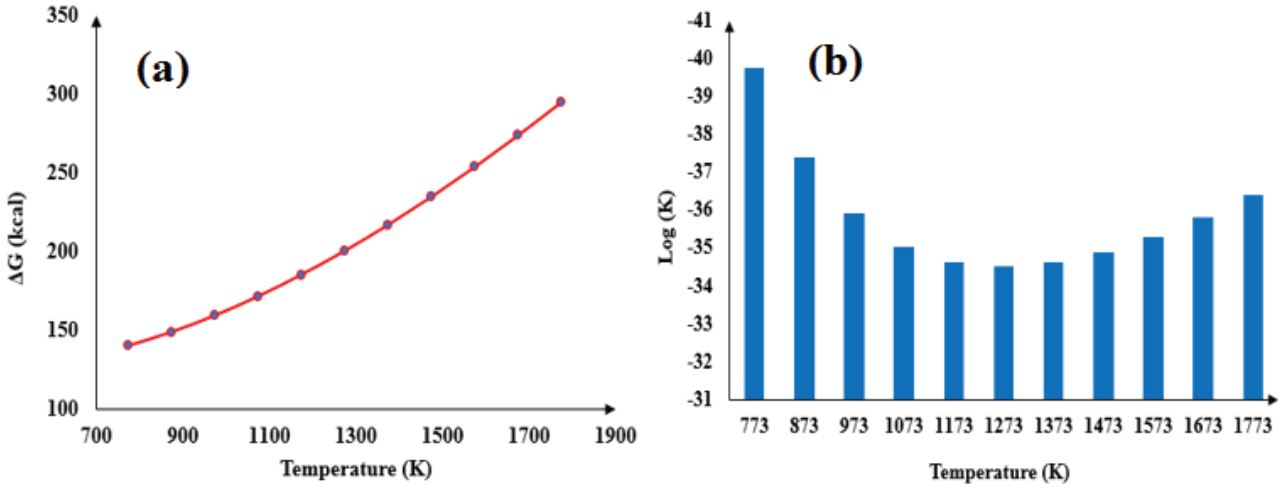

Figure 11. (a) Change in Gibbs free energy as a function of reduction temperature& (b) oxygen partial pressure in the inert gas at reduction temperature

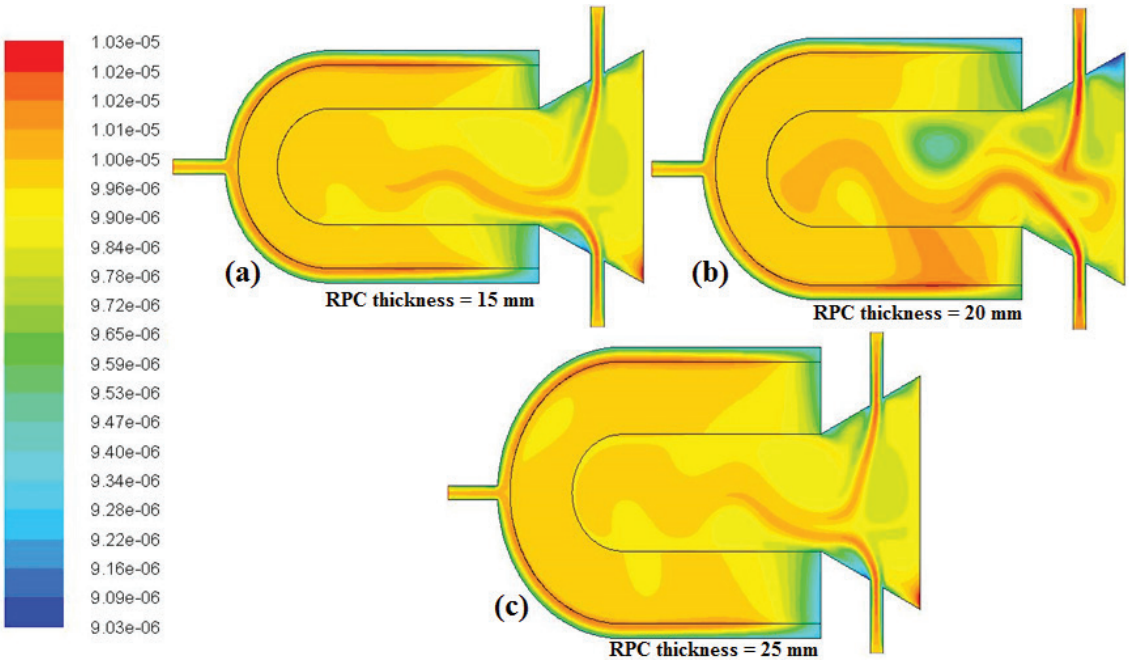

Figure 12. Molar fraction contours of Oxygen.

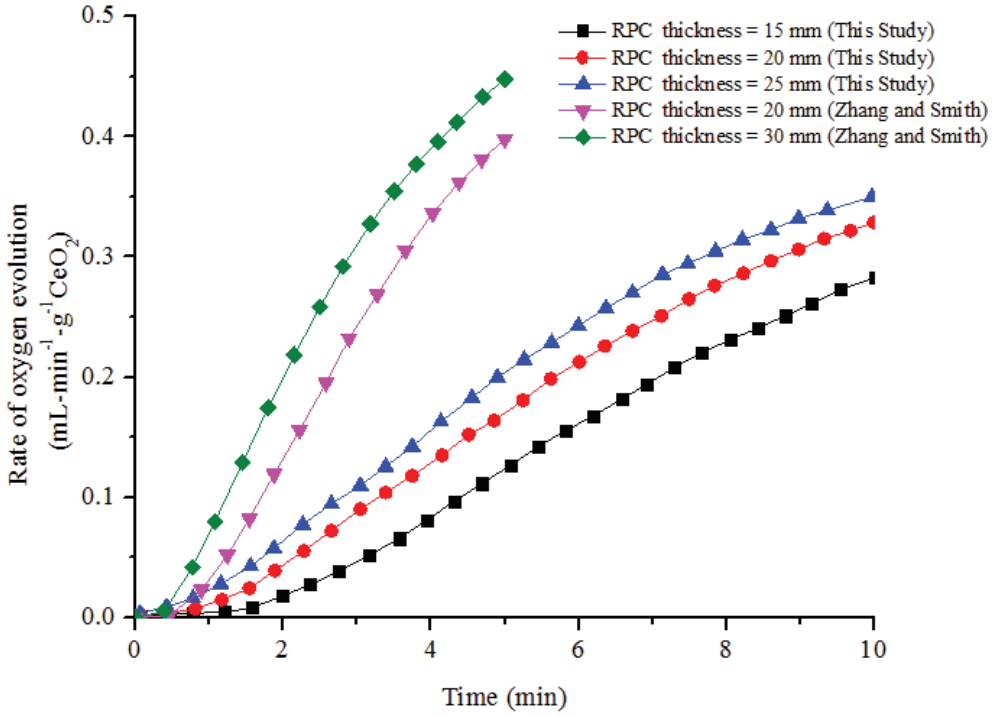

Figure 13. Oxygen evolution rates plot in the CeO_2 reduction process.

mins has been plotted in Figure 10 (3). The temperature profiles of all three RPC thickness clearly indicate that the *15 mm* RPC thickness achieve the highest temperature among all three porous media thicknesses, which is indistinctively consistent with the flux profiles and steady state heat transfer results. Time dependent oxygen concentration at peak oxygen evolution has been shown in Figure 13. It has been observed that the RPC zone exposed to higher temperature tends to reach peak value of oxygen concentration. The oxygen evolution rates for different RPC thicknesses for this study has been plotted in Figure 13 and compared with the Zhang et al. [102].The study performed by Zhang et al. [102] reported the oxygen evolution about *0.929 mL/gCeO$_2$* and *1.184 mL/gCeO$_2$* in *5* minutes for the *20mm* and *30mm* RPCs, respectively. However, when the ceria mass loading is taken into account the oxygen evolution in *5* minutes goes up to *1179.8 mL* and *1973.6 mL* and the theoretical solar-to-fuel efficiency is *9.5%* and *15.9%* (without heat recovery) for *20 mm* and *30 mm*, respectively.while in this study, the RPC zone having *25 mm* thickness yields the highest rate of oxygen evolution, about *0.34 mL/min/gCeO$_2$*. The total amount of oxygen generation for all three RPC thickness in 10 mins is about *1.422 mL/gCeO$_2$*, *1.645 mL/gCeO$_2$* and *1.764 mL/gCeO$_2$* for *15mm, 20mm* and *25 mm*, respectively. However, the total amount of oxygen evolution for the period of *10* mins goes up to*1578.42 mL*, *2434.6 mL* and *3263.4 mL* for *15 mm, 20 mm* and *25 mm*, respectively, when the ceria mass loading is taken into account. According to the eq. (4), solar-to-fuel conversion efficiency is the function of Stoichiometric fuel production rate (r_{fuel}) which is assumed as $r_{CO} = 2r_{O_2}$, HHV of fuel (*286 kJ/mole*) and input solar power (*Q*). Solar-to-fuel efficiencies for the presented three cases are estimated to be *7.82%, 12.07%* and *16.18%* for *15 mm, 20 mm* and *25 mm* of RPC thickness, respectively without heat recovery taken into account.

CONCLUSION

We have presented a numerical model of high-temperature solar thermochemical reactor of hybrid cavity shape that couples the Monte Carlo Ray Tracing (MCRT) technique with computational fluid dynamics (CFD). The influences of RPC thickness on solar-to-fuel conversion efficiency in a solar thermochemical reactor cavity has been explored by means of steady state and transient CFD models. MCRT was applied using SolTrace software to generate the solar flux profile and it was coupled with CFD module to study the heat transfer and concentrated solar flux distribution in the STCR cavity. The conclusions have been drawn as follows;

- The heat transfer inside the cavity and in the porous region (fluid-to-solid) is highly affected by the gas flow gap size which ultimately influences the inert gas flow pattern.
- Among all three porous media thicknesses case considered, the *15 mm* RPC thickness shows a very uniform distribution of solar heat flux as well as achieves the highest temperature.

- Larger gas flow gap allows the fluid to flow slower at given velocity thus cooling the porous region rapidly which results in undesired distribution of temperature in the RPC zone.
- The concentrated flux distribution is uniform in the STCR cavity for all three RPC thicknesses. Even though, the temperature profiles are barely different for varying RPC thicknesses, the thinner RPC zone attains the highest temperature could be considered as an advantage.
- For the two-step H_2O splitting process, the RPC thickness with *25 mm* attains the highest oxygen evolution rate as well as yields the highest solar-to-fuel conversion efficiency, among all three cases considered.
- The RPC zone subjected to higher temperature attains the peak value of O_2 concentration. However, the ceria mass loading is a factor plays a significant role in rate of H_2 production rate. The RPC zone having 25 mm thickness yields the highest rate of *0.34 mL/min/gCeO*$_2$ oxygen evolution.
- For RPC thickness *15 mm, 20 mm* and *25 mm* yield about *1.422 mL/gCeO*$_2$*, 1.645 mL/gCeO*$_2$ and *1.764 mL/gCeO*$_2$ oxygen in *10* min cycle, respectively and when the ceria mass load is considered the total oxygen evolution goes up to *1578.42 mL, 2434.6 mL* and *3263.4 mL*, respectively.
- Solar-to-fuel efficiencies for *15 mm, 20 mm* and *25 mm* RPC thickness are estimated to be *7.82%, 12.07%* and *16.18%,* respectively without heat recovery.

FUTURE WORK RECOMMENDATION

To improve the solar-to-fuel conversion efficiency of two-step H_2O/CO_2 splitting cycle, optical-thermal analysis and cavity shape optimization plays an important role. It's crucial to choose the perfect cavity shape to achieve the uniform distribution of solar flux inside the cavity to achieve the optimum temperature to carry out the redox reactions efficiently. Thus, future/upcoming research papers are/ will be based on optical-thermal analysis and STCR cavity shape optimization in combination with varying geometrical parameters.

NOMENCLATURE

A	area (m^2)
d	collector aperture diameter (m)
f	focal length (m)
F	force (N)
Fs	particle surface force (N)
g	gravitational acceleration (m/s^2)
G	Incident radiative heat flux (W/m^2)
h	collector height (m)
I	radiative intensity (W/m^2)
k	thermal conductivity (W/m-K)
k_a	absorption coefficient (1/m)
k_{pa}	particle absorption coefficient (1/m)
k_{ps}	particle scattering coefficient (1/m)
k_{red}	reduction rate coefficient
k_s	scattering coefficient (1/m)
p	pressure (Pa)
q_r	re-radiation (W/m^2)
Q	heat amount (J)
$Q_{a,p}$	absorption efficiency of particle
r	reaction rate (mol/s)
rπ	parcel position
s	distance in Ω direction
S	source term (W/m^3)
T	temperature (K)
v	velocity (m/s)
V	volume (m^3)
Yi	component concentration
$\dot{m}_p$	particle mass transfer rate (kg/s)
$S_{m,O2}$	mass source term
S_p	fluid pressure drop source term
d_s	mean cell size (mm)
S_h	convective heat transfer source term
h_v	volumetric convection heat transfer coefficient
Ss	Volumetric heat source term

Greek Symbols

β	extinction coefficient
δ	non-stoichiometric coefficient
δ_p	Dirac delta function
η	efficiency
μ	dynamic viscosity (Pa s)
ρ	density (kg/m^3)
σ	Stefan-Boltzmann constant $W/(m^2K^4)$
ψ	angle (rad)
Ω	solid angle(rad)
ϕ	porosity
λeff	Effective thermal conductivity

Subscripts

b	body
conv	convection
E	energy
f	Fluid
f_p	fluid-particle interphase
fs	fluid-solid interphase
fuel	chemical fuel
m	mass
p	particles
p_b	particle black body
q	quartz glass
rad	radiation
reac	reaction
rim	Rim
s	solid
solar	solar energy

t	total
th	thermal
i	Initial
f	Final

Abbreviation

CFD	Computational fluid dynamics
DEM	Discrete element method
DNI	Direct normal irradiance
DOM	Discrete ordinate method
HHV	Higher heating value
STCR	Solar thermochemical reactor
RPC	Reticulated porous ceramic

AUTHORSHIP CONTRIBUTIONS

Authors equally contributed to this work.

DATA AVAILABILITY STATEMENT

The authors confirm that the data that supports the findings of this study are available within the article. Raw data that support the finding of this study are available from the corresponding author, upon reasonable request.

CONFLICT OF INTEREST

The author declared no potential conflicts of interest with respect to the research, authorship, and/or publication of this article.

ETHICS

There are no ethical issues with the publication of this manuscript.

REFERENCES

[1] Xu RJ, Zhang XH, Wang RX, Xu SH, Wang HS. Experimental investigation of a solar collector integrated with a pulsating heat pipe and a compound parabolic concentrator. Energy Convers Manag 2017;148:68−77. [CrossRef]

[2] Jamal-Abad MT, Saedodin S, Aminy M. Experimental investigation on a solar parabolic trough collector for absorber tube filled with porous media. Renew Energy 2017;107:156−163. [CrossRef]

[3] Michalsky R, Parman BJ, Amanor-Boadu V, Pfromm PH. Solar thermochemical production of ammonia from water, air and sunlight: Thermodynamic and economic analyses. Energy 2012;42:251−260. [CrossRef]

[4] Baykara SZ. Hydrogen production by direct solar thermal decomposition of water, possibilities for improvement of process efficiency. Int J Hydrog Energy 2004;29:1451−1458. [CrossRef]

[5] Loutzenhiser PG, Meier A, Steinfeld A. Review of the Two-Step H2O/CO2-Splitting solar thermochemical cycle based on Zn/ZnO redox reactions. Materials 2010;3:4922−4938. [CrossRef]

[6] Smestad GP, Steinfeld A. Review: Photochemical and thermochemical production of solar fuels from H2O and CO2 using metal oxide catalysts. Ind Eng Chem Res 2012;51:11828−11840. [CrossRef]

[7] Miller JE, McDaniel AH, Allendorf MD. Considerations in the design of materials for solar-driven fuel production using metal-oxide thermochemical cycles. Adv Energy Mater 2014;4:1−19. [CrossRef]

[8] Lapp J, Davidson JH, Lipiński W. Heat transfer analysis of a Solid-solid heat recuperation system for solar-driven nonstoichiometric redox cycles. J Sol Energy Eng 2013;135:031004. [CrossRef]

[9] Diver RB, Miller JE, Allendorf MD, Siegel NP, Hogan RE. Solar thermochemical water-splitting ferrite-cycle heat engines. J Sol Energy Eng 2008;130:041001. [CrossRef]

[10] Kaneko H, Miura T, Fuse A, Ishihara H, Taku S, Fukuzumi H, et al. Rotary-type solar reactor for solar hydrogen production with two-step water splitting process. Energy Fuels 2007;21:2287−2293. [CrossRef]

[11] Scheffe JR, Welte M, Steinfeld A. Thermal reduction of ceria within an aerosol reactor for H2O and CO2 splitting. Ind Eng Chem Res 2014;53:2175−2182. [CrossRef]

[12] Abanades S, Flamant G. Thermochemical hydrogen production from a two-step solar-driven water-splitting cycle based on cerium oxides. Sol Energy 2006;80:1611−1623. [CrossRef]

[13] Ermanoski I, Siegel NP, Stechel EB. A new reactor concept for efficient solar-thermochemical fuel production. J Sol Energy Eng 2013;135:031002. [CrossRef]

[14] Kodama T, Enomoto S, Hatamachi T, Gokon N. Application of an internally circulating fluidized bed for windowed solar chemical reactor with direct irradiation of reacting particles. J Sol Energy Eng 2008;130:014504. [CrossRef]

[15] Brendelberger S, Rosenstiel A, Lopez-Roman A, Prieto C, Sattler C. Performance analysis of operational strategies for monolithic receiver-reactor arrays in solar thermochemical hydrogen production plants. Int J Hydrog Energy 2020;45:26104−26116. [CrossRef]

[16] Zoller S, Koepf E, Roos P, Steinfeld A. Heat transfer model of a 50 kW solar receiver-reactor for thermochemical redox cycling using cerium dioxide. J Sol Energy Eng 2019;141. [CrossRef]

[17] Garnier JE, Blumenthal RN, Panlener RJ, Sharma RK. A thermodynamic study on CaO-doped nonstoichiometric cerium dioxide. J Phys Chem Solids 1976;37:368−378. [CrossRef]

[18] Zinkevich M, Djurovic D, Aldinger F. Thermodynamic modelling of the cerium-oxygen system. Solid State Ion 2006;177:989−1001. [CrossRef]
[19] Lapp J, Davidson JH, Lipiński W. Efficiency of two-step solar thermochemical non-stoichiometric redox cycles withheat recovery. Energy 2012;37:591−600. [CrossRef]
[20] Scheffe JR, Steinfeld A. Oxygen exchange materials for solar thermochemical splitting of H2O and CO2: A review. Mater Today 2014;17:341−348. [CrossRef]
[21] Bulfin B, Lowe AJ, Keogh KA, Murphy BE, Lübben O, Krasnikov SA, Shvets IV. Analytical model of CeO2 oxidation and reduction. J Phys Chem C 2013;117:24129−24137. [CrossRef]
[22] Farooqui A, Bose A, Ferrero D, Llorca J, Santarelli M. Simulation of two-step redox recycling of non-stoichiometric ceria with thermochemical dissociation of CO 2 /H 2 O in moving bed reactors - Part I: Model development with redox kinetics and sensitivity analysis. Chem Eng Sci 2019;226:114873. [CrossRef]
[23] Li S, Kreider PB, Wheeler VM, Lipinski W. Thermodynamic analyses of fuel production via solar-driven ceria-based nonstoichiometric redox cycling: A Case study of the isothermal membrane reactor system. J Sol Energy Eng 2019;141:021012. [CrossRef]
[24] Anikeev VI, Kirillov VA. Basic design principles and some methods of investigation of catalytic reactors-receivers of solar radiation. Sol Energy Mater 1991;24:633−646. [CrossRef]
[25] Gokon N, Kumaki S, Miyaguchi Y, Bellan S, Kodama T, Cho H. Development of a 5kW th internally circulating fluidized bed reactor containing quartz sand for continuously-fed coal-coke gasification and a beam-down solar concentrating system. Energy 2019;166:1−16. [CrossRef]
[26] Yu T, Yuan Q, Lu J, Ding J, Lu Y. Thermochemical storage performances of methane reforming with carbon dioxide in tubular and semi-cavity reactors heated by a solar dish system. Appl Energy 2017;185:1994−2004. [CrossRef]
[27] Bader R, Chandran RB, Venstrom LJ, Sedler SJ, Krenzke PT, De Smith RM, et al. Design of a solar reactor to split CO2 via isothermal redox cycling of ceria. J Sol Energy Eng Trans 2015;137:031007. [CrossRef]
[28] Lichty P, Liang X, Muhich C, Evanko B, Bingham C, Weimer AW. Atomic layer deposited thin film metal oxides for fuel production in a solar cavity reactor. Int J Hydrog Energy 2012;37:16888−16894. [CrossRef]
[29] Chambon M, Abanades S, Flamant G. Thermal dissociation of compressed ZnO and SnO2 powders in a moving-front solar thermochemical reactor. AIChE J 2011;57:2264−2273. [CrossRef]
[30] Schunk LO, Haeberling P, Wept S, Wuillemin D, Meier A, Steinfeld A. A receiver-reactor for the solar thermal dissociation of zinc oxide. J Sol Energy Eng 2008;130:021009. [CrossRef]
[31] Chueh WC, McDaniel AH, Grass ME, Hao Y, Jabeen N, Liu Z, et al. Highly enhanced concentration and stability of reactive Ce 3+ on doped CeO 2 surface revealed in operando. Chem Mater 2012;24:1876−1882. [CrossRef]
[32] Lapp J, Davidson J, Lipiński W. Heat transfer analysis of a solid-solid heat recuperation system for solar-driven non-stoichiometric redox cycles. J Sol Energy Eng 2013;135:031004. [CrossRef]
[33] Miller JE, Allendorf MD, Ambrosini A, Chen KS, Coker EN, Dedrick DE, et al. Final Report Reimagining Liquid Transportation Fuels : Sunshine to Petrol; Sandia National Laboratories, Albuquerque, NM, Report No. SAND2012−0307', 2012.
[34] Keykhah S, Assareh E, Moltames R, Taghipour A, Barati H. Thermoeconomic analysis and multi-objective optimization of an integrated solar system for hydrogen production using particle swarm optimization algorithm. J Therm Eng 2021;7:746−760. [CrossRef]
[35] Ghodbane M, Boumeddane B, Hussein A, Li D, Sivasankaran S. Optical numerical investigation of a solar power plant of parabolic trough collectors. J Therm Eng 2021;7:550−569. [CrossRef]
[36] Lougou BG, Han D, Zhang H, Jiang B, Anees J, Ahouannou C, et al. Numerical and experimental analysis of reactor optimum design and solar thermal-chemical energy conversion for multi-disciplinary applications. Energy Convers Manag 2020;213:112870. [CrossRef]
[37] Safari F, Dincer I. A review and comparative evaluation of thermochemical water splitting cycles for hydrogen production. Energy Convers Manag 2020;205:112182. [CrossRef]
[38] Bhosale RR, Kumar A, Sutar P. Thermodynamic analysis of solar driven SnO2/SnO based thermochemical water splitting cycle. Energy Convers Manag 2017;135:226−235. [CrossRef]
[39] Chen X, Wang F, Han Y, Yu R, Cheng Z. Thermochemical storage analysis of the dry reforming of methane in foam solar reactor. Energy Convers Manag 2018;158:489−498. [CrossRef]
[40] Wang F, Tan J, Ma L, Leng Y. Effects of key factors on solar aided methane steam reforming in porous medium thermochemical reactor. Energy Convers Manag 2015;103:419−430. [CrossRef]
[41] Wang F, Tan J, Shuai Y, Gong L, Tan H. Numerical analysis of hydrogen production via methane steam reforming in porous media solar thermochemical reactor using concentrated solar irradiation as heat source. Energy Convers Manag 2014;87:956−964. [CrossRef]

[42] Charvin P, Stéphane A, Florent L, Gilles F. Analysis of solar chemical processes for hydrogen production from water splitting thermochemical cycles. Energy Convers Manag 2008;49:1547−1556. [CrossRef]
[43] Bhosale R, Kumar A, AlMomani F, Ghosh U, Saad Anis M, Kakosimos K, et al. Solar hydrogen production via a samarium oxide-based thermochemical water splitting cycle. Energies 2016;9:316. [CrossRef]
[44] Bhosale RR, Sutar P, Kumar A, AlMomani F, Ali MH, Ghosh U, et al. Solar hydrogen production via erbium oxide based thermochemical water splitting cycle. J Renew Sustain Energy 2016;8:034702. [CrossRef]
[45] Bhosale R, Kumar A, AlMomani F. Solar Thermochemical hydrogen production via terbium oxide based redox reactions. Int J Photoenergy 2016;2016:1−9. [CrossRef]
[46] Bhosale R, Kumar A, AlMomani F, Gupta RB. Solar thermochemical ZnO/ZnSO4 water splitting cycle for hydrogen production. Int J Hydrog Energy 2017;42:23474−23483. [CrossRef]
[47] Bhosale R, AlMomani F, Takalkar G. Thermodynamic analysis of solar-driven chemical looping steam methane reforming over Cr2O3/Cr redox pair. Int J Hydrog Energy 2020;45:10370−10380. [CrossRef]
[48] Bhosale RR, AlMomani F, Rashid S. Solar thermochemical H2 production via MnSO4/MnO water splitting cycle: Thermodynamic equilibrium and efficiency analysis. Int J Hydrog Energy 2020;45:10324−10333. [CrossRef]
[49] Takalkar GD, Bhosale RR, Kumar A, AlMomani F, Khraisheh M, Shakoor RA, et al. R.B. Transition metal doped ceria for solar thermochemical fuel production. Sol Energy 2018;172:204−211. [CrossRef]
[50] Sarwar J, Georgakis G, Kouloulias K, Kakosimos KE. Experimental and numerical investigation of the aperture size effect on the efficient solar energy harvesting for solar thermochemical applications. Energy Convers Manag 2015;92:331−341. [CrossRef]
[51] Siddiqui O, Ishaq H, Dincer I. A novel solar and geothermal-based trigeneration system for electricity generation, hydrogen production and cooling. Energy Conver Manag vol. 2019;198:111812. [CrossRef]
[52] Jiang Q, Zhang H, Cao Y, Hong H, Jin H. Solar hydrogen production via perovskite-based chemical-looping steam methane reforming. Energy Convers Manag 2019;187:523−536. [CrossRef]
[53] Sedighi M, Padilla RV, Taylor RA, Lake M, Izadgoshasb I, Rose A. 'High-temperature, point-focus, pressurised gas-phase solar receivers: A comprehensive review. Energy Convers Manag 2019;185:678−717. [CrossRef]
[54] Lee H, Kim A, Lee B, Lim H. Comparative numerical analysis for an efficient hydrogen production via a steam methane reforming with a packed-bed reactor, a membrane reactor, and a sorption-enhanced membrane reactor. Energy Convers Manag 2020;213:112839. [CrossRef]
[55] Wang Y, Liu Q, Sun J, Lei J, Ju Y, Jin H. A new solar receiver/reactor structure for hydrogen production. Energy Convers Manag 2017;133:118−126. [CrossRef]
[56] Zhu L, Lu Y, Li F. Reactivity of Ni, Cr and Zr doped ceria in CO2 splitting for CO production via two-step thermochemical cycle. Int J Hydrog Energy 2018;43:13754−13763. [CrossRef]
[57] Teknetzi I, Nessi P, Zaspalis V, Nalbandian L. Ni-ferrite with structural stability for solar thermochemical H2O/CO2 splitting. Int J Hydrog Energy 2017;42:26231−26242. [CrossRef]
[58] Guene Lougou B, Hong J, Shuai Y, Huang X, Yuan Y, Tan H. Production mechanism analysis of H2 and CO via solar thermochemical cycles based on iron oxide (Fe3O4) at high temperature. Sol Energy 2017;148:117−127. [CrossRef]
[59] Muhich CL, Blaser S, Hoes MC, Steinfeld A. Comparing the solar-to-fuel energy conversion efficiency of ceria and perovskite based thermochemical redox cycles for splitting H2O and CO2. Int J Hydrog Energy 2018;43:18814−18831. [CrossRef]
[60] Wu S, Zhou C, Doroodchi E, Nellore R, Moghtaderi B. A review on high-temperature thermochemical energy storage based on metal oxides redox cycle. Energy Convers Manag 2018;168:421−453. [CrossRef]
[61] Alovisio A, Chacartegui R, Ortiz C, Valverde JM, Verda V. Optimizing the CSP-calcium looping integration for thermochemical energy storage. Energy Convers Manag 2017;136:85−98. [CrossRef]
[62] Pan ZH, Zhao CY. Gas-solid thermochemical heat storage reactors for high-temperature applications. Energy 207;130:155−173. [CrossRef]
[63] Liu T, Liu Q, Lei J, Sui J, Jin H. Solar-clean fuel distributed energy system with solar thermochemistry and chemical recuperation. Appl Energy 2018;225:380−391. [CrossRef]
[64] de la Calle A, Bayon A. Annual performance of a thermochemical solar syngas production plant based on non-stoichiometric CeO 2. Int J Hydrog Energy 2019;44:1409−1424. [CrossRef]
[65] Dincer I, Acar C. Innovation in hydrogen production. Int J Hydrog Energy 2017;42:14843−14864. [CrossRef]
[66] Banerjee A, Chandran RB, Davidson JH. Experimental investigation of a reticulated porous alumina heat exchanger for high temperature gas heat recovery. Appl Therm Eng 2015;75:889−895. [CrossRef]
[67] Bala Chandran R, De Smith RM, Davidson JH. Model of an integrated solar thermochemical reactor/reticulated ceramic foam heat exchanger for gas-phase heat recovery. Int J Heat Mass Transf 2015;81:404−414. [CrossRef]
[68] Chandran RB, Bader R, Lipiński W. Transient heat and mass transfer analysis in a porous ceria structure of a novel solar redox reactor. Int J Therm Sci 2015;92:138−149. [CrossRef]

[69] Chen X, Wang F, Yan X, Cheng Z, Han Y, Jie Z. Thermal and chemical analysis of methane dry reforming in a volumetric reactor under highly concentrated solar radiation. Sol Energy 2018;162:187−195. [CrossRef]
[70] Chen X, Wang F, Yan X, Han Y, Cheng Z, Jie Z. Thermochemical performance of solar driven CO 2 reforming of methane in volumetric reactor with gradual foam structure. Energy 2018;151:545−555. [CrossRef]
[71] Furler P, Steinfeld A. Heat transfer and fluid flow analysis of a 4kW solar thermochemical reactor for ceria redox cycling. Chem Eng Sci 2015;137:373−383. [CrossRef]
[72] Kong H, Hao Y, Jin H. Isothermal versus two-temperature solar thermochemical fuel synthesis: A comparative study. Appl Energy 2018;228:301−308. [CrossRef]
[73] Agrafiotis C, Becker A, Roeb M, Sattler C. Exploitation of thermochemical cycles based on solid oxide redox systems for thermochemical storage of solar heat. Part 5: Testing of porous ceramic honeycomb and foam cascades based on cobalt and manganese oxides for hybrid sensible/thermochemical heat storage. Sol Energy 2016;139:676−694. [CrossRef]
[74] Bachirou GL, Yong S, RuMing P, Gédéon C, Clément A, Hao Z, et al. Radiative heat transfer and thermal characteristics of Fe-based oxides coated SiC and Alumina RPC structures as integrated solar thermochemical reactor. Sci China Technol Sci 2018;61:1788−1801. [CrossRef]
[75] Mendes MAA, Talukdar P, Ray S, Trimis D. Detailed and simplified models for evaluation of effective thermal conductivity of open-cell porous foams at high temperatures in presence of thermal radiation. Int J Heat Mass Transf 2014;68:612−624. [CrossRef]
[76] Du S, Li MJ, Ren Q, Liang Q, He YL. Pore-scale numerical simulation of fully coupled heat transfer process in porous volumetric solar receiver. Energy 2017;140:1267−1275. [CrossRef]
[77] Kogawa T, Chen L, Okajima J, Sakurai A, Komiya A, Maruyama S. Effects of concentration of participating media on turbulent natural convection in cubic cavity. Appl Therm Eng 2018;131:141−149. [CrossRef]
[78] Zhu Q, Xuan Y. Pore scale numerical simulation of heat transfer and flow in porous volumetric solar receivers. Appl Therm Eng 2017;120:150−159. [CrossRef]
[79] Nimvari ME, Jouybari NF, Esmaili Q. A new approach to mitigate intense temperature gradients in ceramic foam solar receivers. Renew Energy 2018;122:206−215. [CrossRef]
[80] Valadés-Pelayo PJ, Arancibia-Bulnes CA. Transient behavior of a multi-tubular cavity solar thermochemical reactor. Appl Therm Eng 2017;123:1255−1262. [CrossRef]
[81] Chen X, Xia XL, Yan XW, Sun C. Heat transfer analysis of a volumetric solar receiver with composite porous structure. Energy Convers Manag 2017;136:262−269. [CrossRef]
[82] Guene Lougou B, Shuai Y, Guohua Z, Chaffa G, Ahouannou C, Tan H. Analysis of H2 and CO production via solar thermochemical reacting system of NiFe2O4 redox cycles combined with CH4 partial oxidation. Int J Hydrog Energy 2018;43:5996−6010. [CrossRef]
[83] Bayat N, Rezaei M, Meshkani M. Methane decomposition over Ni-Fe/Al2O3 catalysts for production of COx-free hydrogen and carbon nanofiber. Int J Hydrog Energy 2016;41:1574−1584. [CrossRef]
[84] Muhich CL, Ehrhart BD, Witte VA, Miller SL, Coker EN, Musgrave CB, et al. Predicting the solar thermochemical water splitting ability and reaction mechanism of metal oxides: A case study of the hercynite family of water splitting cycles. Energy Environ Sci 2015;8:3687−3699. [CrossRef]
[85] Gokon N, Suda T, Kodama T. Oxygen and hydrogen productivities and repeatable reactivity of 30-mol%-Fe-, Co-, Ni-, Mn-doped CeO2-δ for thermochemical two-step water-splitting cycle. Energy 2015;90:1280−1289. [CrossRef]
[86] Roberts SJ, Carr NG, McLaughlin J, Hagelin-Weaver HE. Iron precipitated onto ceria-zirconia nanoparticle mixtures for the production of hydrogen via two-step thermochemical water splitting. Int J Hydrog Energy 2018;43:12970−12984. [CrossRef]
[87] Reich L, Bader R, Simon T, Lipiński W. Thermal transport model of a packed-bed reactor for solar thermochemical CO2 capture. Spec Top Rev Porous Media 2015;6:197−209. [CrossRef]
[88] Haussener S, Hirsch D, Perkins C, Weimer A, Lewandowski A, Steinfeld A. Modeling of a multitube high-temperature solar thermochemical reactor for hydrogen production. J Sol Energy Eng 2009;131;024503. [CrossRef]
[89] Ishida T, Gokon N, Hatamachi T, Kodama T. Kinetics of thermal reduction step of thermochemical two-step water splitting using CeO2 particles: Master-plot method for analyzing non-isothermal experiments. Energy Procedia 2014;49:1970−1979. [CrossRef]
[90] Wu Z, Caliot C, Flamant G, Wang Z. Coupled radiation and flow modeling in ceramic foam volumetric solar air receivers. Sol Energy 2011;85:2374−2385. [CrossRef]
[91] Vafai K. Handbook of Porous Media. 3rd ed. Boca Raton: CRC Press; 2015. [CrossRef]
[92] Modest MF. Radiative heat transfer. 3rd ed. Amsterdam: Elsevier; 2013. [CrossRef]
[93] Hsu PF, Howell JR. Measurements of thermal conductivity and optical properties of porous partially stabilized zirconia. Exp Heat Transf 1992;5:293−313. [CrossRef]

[94] Keshtkar MM, Nassab SG. Theoretical analysis of porous radiant burners under 2-D radiation field using discrete ordinates method. J Quant Spectrosc Radiat Transf 2009;110:1894−1907. [CrossRef]

[95] Furler P, Scheffe J, Gorbar M, Moes L, Vogt U, Steinfeld A. Solar thermochemical CO2 splitting utilizing a reticulated porous ceria redox system. Energy Fuels 2012;26:7051−7059. [CrossRef]

[96] Suter S, Steinfeld A, Haussener S. Pore-level engineering of macroporous media for increased performance of solar-driven thermochemical fuel processing. Int J Heat Mass Transf 2014;78:688−698. [CrossRef]

[97] Nagashima A. Thermophysical properties of high temperature liquids. Netsu Bussei 1990;4:69−76. [CrossRef]

[98] Jilte R, Ahmadi MH, Kalamkar V, Kumar R. Solar flux distribution study in heat pipe cavity receiver integrated with biomass gasifier. Int J Energy Res 2020;44:7698−7712. [CrossRef]

[99] Shuai Y, Xia XL, Tan HP. Radiation performance of dish solar concentrator/cavity receiver systems. Sol Energy 2008;82:13−21. [CrossRef]

[100] Lee H. The geometric-optics relation between surface slope error and reflected ray error in solar concentrators. Sol Energy 2014;101:299−307. [CrossRef]

[101] Zhang H, Lougou BG, Pan R, Shuai Y, Wang F, Cheng Z, et al. Analysis of thermal transport and fluid flow in high-temperature porous media solar thermochemical reactor. Sol Energy 2018;173:814−824. [CrossRef]

[102] Zhang H, Smith JD. Investigating influences of geometric factors on a solar thermochemical reactor for two-step carbon dioxide splitting via CFD models. Sol Energy 2019;188:935−950. [CrossRef]